Czech Technical University in Prague
Faculty of Nuclear Sciences and Physical Engineering

Department of Physics
Study program: Nuclear and Particle Physics

Anisotropic flow fluctuations in heavy-ion collisions at the LHC

DIPLOMA THESIS

Author: Bc. Tomáš Poledníček
Supervisor: prof. Dr. Boris Tomášik
Academic year: 2023

České vysoké učení technické v Praze
Fakulta jaderná a fyzikálně inženýrská

Katedra fyziky
Studijní program: Jaderná a částicová fyzika

Fluktuace anizotropního toku ve srážkách těžkých iontů na LHC

DIPLOMOVÁ PRÁCE

Vypracoval: Bc. Tomáš Poledníček
Vedoucí práce: prof. Dr. Boris Tomášik
Rok: 2023

FAKULTA JADERNÁ A FYZIKÁLNĚ INŽENÝRSKÁ

KATEDRA FYZIKY

ZADÁNÍ DIPLOMOVÉ PRÁCE

Akademický rok: 2022/2023

Student:	Bc. Tomáš Poledníček
Studijní program:	Jaderná a částicová fyzika
Název práce: (česky)	Fluktuace anizotropního toku ve srážkách těžkých iontů na LHC
Název práce: (anglicky)	Anisotropic flow fluctuations in heavy-ion collisions at the LHC
Jazyk práce:	Angličtina

Pokyny pro vypracování:

1) Nastavte hybridní model s hydrodynamickou částí tak, aby byly reprodukovány jednočásticové rozdělení ze srážek Pb+Pb při energiích LHC

2) Prostudujte dostupná experimentální data ohledem anizotropního toku a jeho fluktuací, fluktuací úhlu toku, korelací mezi jednotlivými řády a multiharmonických korelací.

3) Připravte přehled experimentální situace ohledem anizotropie toku

4) Ze simulací získejte informaci o anizotropním toku, jeho fluktuacích, fluktuacích úhlu toku a multiharmonických korelací.

Doporučená literatura:

[1] S. Acharya et al. (ALICE collaboration): JHEP 05 (2020) 085

[2] S. Acharya et al. (ALICE collaboration): Phys. Lett. B 818 (2021) 136354

[3] ALICE collaboration: arXiv 2206.04587

[4] ALICE collaboration: arXiv 2206.04574

Jméno a pracoviště vedoucího diplomové práce:

prof. Dr. Boris Tomášik
Katedra fyziky, Fakulta jaderná a fyzikálně inženýrská ČVUT v Praze

Datum zadání diplomové práce: 20.10.2022

Termín odevzdání diplomové práce: 03.05.2023

Doba platnosti zadání je dva roky od data zadání.

.....
garant studijního programu

.....
vedoucí katedry

.....
děkan

V Praze dne 20.10.2022

ČESKÉ VYSOKÉ UČENÍ TECHNICKÉ V PRAZE

Fakulta jaderná a fyzikálně inženýrská

Břehová 7
115 19 Praha 1

P R O H L Á Š E N Í

Já, níže podepsaný

Jméno a příjmení studenta:	Tomáš Poledníček
Osobní číslo:	486381
Název studijního programu (oboru):	Jaderná a částicová fyzika

prohlašuji, že jsem diplomovou práci s názvem:

Fluktuace anizotropního toku ve srážkách těžkých iontů na LHC

vypracoval samostatně a uvedl veškeré použité informační zdroje v souladu s Metodickým pokynem o dodržování etických principů při přípravě vysokoškolských závěrečných prací.

V Praze dne 2. 5. 2023 ……*Poledníček*……

podpis

Acknowledgments

It is my honourable duty to thank prof. Dr. Boris Tomášik for help in leading, compiling, patience, formulating tasks, providing professional materials and scientific guidance in solving the tasks of my master thesis. Many thanks to Iurii Karpenko, Ph.D. and Ing. Jakub Cimerman for invaluable technical assistance and professional advice.

Bc. Tomáš Poledníček

Název práce:
Fluktuace anizotropního toku ve srážkách těžkých iontů na LHC

Autor: Bc. Tomáš Poledníček

Studijní program: Jaderná a částicová fyzika
Druh práce: Diplomová práce

Vedoucí práce: prof. Dr. Boris Tomášik
Katedra Fyziky, Fakulta jaderná a fyzikálně inženýrská, České vysoké učení technické v Praze
Konzultant: Iurii Karpenko, Ph.D.
Katedra Fyziky, Fakulta jaderná a fyzikálně inženýrská, České vysoké učení technické v Praze

Abstrakt: Srážky těžkých iontů nám umožňují vznik husté hmoty, která existovala několik mikrosekund po velkém třesku. Tato exotická tekutina se nazývá kvark-gluonové plazma (QGP). Hydrodynamický popis srážek těžkých iontů v posledních letech ukázal sílu a jednoduchost. Hydrodynamický přístup umožňuje simulovat a pochopit dynamiku jaderných srážek z hlediska makroskopických veličin, jako je hustota energie, teplota a tlak. Vytváří také přímou vazbu na stavovou rovnici a umožňuje tak přímo studovat, jak konkrétní stavová rovnice ovlivňuje pozorovatelné veličiny. V této práci se zaměřujeme na kalibraci hybridního hydrodynamického modelu pro srážky Pb+Pb při CERN LHC energiích, konkrétně $\sqrt{s_{NN}} = 2.76$ TeV a $\sqrt{s_{NN}} = 5.02$ TeV, a fluktuacemi anizotropního toku.
Klíčová slova: hydrodynamické modelování, eliptický tok, fluktuace anizotropního toku

Title:
Anisotropic flow fluctuations in heavy-ion collisions at the LHC

Author: Bc. Tomáš Poledníček

Abstract: Heavy ion collisions allow us to study dense matter, which existed several microseconds after the Big Bang. This exotic fluid is called quark-gluon plasma (QGP). The development of hydrodynamic descriptions of heavy ion collisions in recent years has shown their power and simplicity. The hydrodynamic approach makes it possible to simulate and understand the dynamics of nuclear collisions in terms of macroscopic quantities such as energy density, temperature and pressure. It also creates a direct link to the equation of state and thus allows to directly study how a particular equation of state affects observable quantities. In this work we focus on the calibration of hybrid hydrodynamic model for Pb+Pb collisions at CERN LHC energies, namely $\sqrt{s_{NN}} = 2.76$ TeV and $\sqrt{s_{NN}} = 5.02$ TeV, and anisotropic flow fluctuation.
Key words: hydrodynamic modelling, elliptic flow, anisotropic flow fluctuations

Contents

Introduction

Particle physics is a fascinating field that aims to explore the fundamental building blocks of our universe. Among the key areas of research in particle physics is the study of the early stages of the universe, which allows physicists to answer questions about the Big Bang. One of the ways this is done is by studying strongly interacting matter, which includes the hot and dense quark-gluon plasma (QGP) that existed just after the Big Bang.

QGP is an exotic fluid that can be observed in the collisions of neutron stars and in the creation of matter during the formation of the universe. On Earth, scientists study QGP through experiments involving heavy ion collisions, such as those conducted at the LHC accelerator at CERN or the RHIC at BNL.

Relativistic fluid dynamics is an important tool to study various phenomena in astrophysics and nuclear physics. It provides a useful framework for understanding the evolution of QGP in ultra-relativistic heavy ion collisions and the behaviour of matter in extreme conditions. For example, it has been applied to the collapse of massive stars, the formation and flow around black holes, and the collisions of neutron stars.

In heavy ion collisions, relativistic flows can result in the creation of a near-perfect fluid with the lowest possible viscosity. This collective behaviour is studied through the measurement of anisotropic flow, such as elliptic flow.

This work provides a comprehensive overview of the physics of heavy ion collisions and the applicability of the hydrodynamic approach to describe the evolution of QGP. It is divided into several chapters, including a discussion of anisotropic flow and the measurement method, a theory of relativistic hydrodynamics suitable for heavy ion collisions, and a summary of hydrodynamic modeling in heavy ion physics. The work also includes a comparison of the results obtained through modeling with experimental data.

Overall, this work provides a valuable contribution to our understanding of the behaviour of matter in extreme conditions and the evolution of our universe.

In this work, natural system of units will be used so that the Planck constant, the speed of light and the Boltzmann constant will be set to one, $\hbar = c = k_b = 1$. All theoretical foundations concerning relativistic hydrodynamics will be explained in four space-time dimensions (3 spatial dimensions and 1 time dimension). The convention used for the metric tensor is $(+, -, -, -)$ and the indices $(\mu, \nu, \lambda \ ...)$ will be used to denote components of space-time vectors.

Chapter 1

Heavy ion collisions

In this work, we will focus on heavy ion collisions at very high energies. The heaviest systems under study are collisions of ^{197}Au and ^{208}Pb.

Among the important research centres that study the relativistic collisions of heavy ions, there are Brookhaven National Laboratory (BNL) located in the United States of America and the European Organisation for Nuclear Research (CERN). Currently, heavy ion collisions are carried out on Relativistic Heavy Ion Collider (RHIC) and Large Hadron Collider (LHC). In the relativistic collisions of heavy ions, a large number of particles is produced. On particle accelerators like RHIC or LHC, nuclei collide at high velocities that are close to the speed of light. Quark-gluon plasma (QGP) is produced at these collisions. QGP is a state in which quarks are not bound in hadrons, in which the Universe was briefly after the Big Bang. [26]

1.1 Quark-Gluon Plasma

Quark-gluon plasma is a dense state that exists at high energies and temperatures. It is believed that it has existed 10 microseconds after the Big Bang. Quark-gluon plasma consists of quarks and gluons. At the high temperature, particles are very close together (less than 1 fm = 10^{-15} m). Mesons and baryons break up to form a mixture of quarks and gluons. In this plasma, the quarks are deconfined.

The main objective of heavy ion collisions is to study quark-gluon plasma and study 2 phase transitions, which are conjectured by quantum chromodynamics. The first of these transitions is deconfinement and the second one is the chiral phase transition. Under normal conditions, quarks are trapped in hadrons. However, if we increase the temperature or increase the baryon density (compression), there may occur a transition in which ordinary hadrons are no longer present and in which quarks and gluons become relevant degrees of freedom. [25, 26]

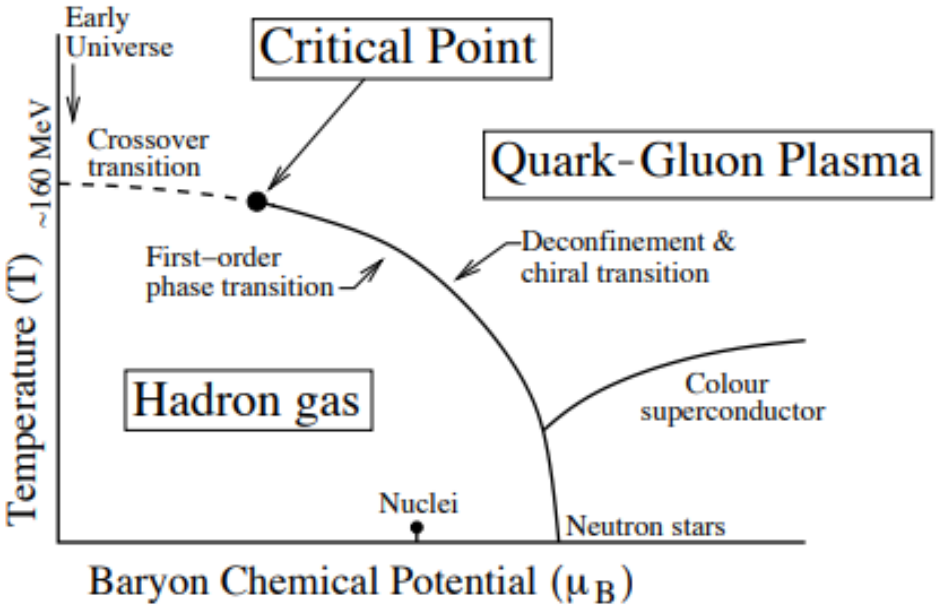

Figure 1.1: The phase diagram of strongly interacting matter taken from [15].

Current experiments in relativistic collisions of heavy ions point to the formation of very dense matter in which quarks and gluons interact. This system exhibits collective behaviour and can be found in compact stars or in the early phase of the Universe.

1.2 Space-time evolution of a heavy ion collision

Heavy ion collisions are highly energetic processes with very characteristic dynamics. The space-time evolution of the two colliding nuclei is shown in Figure 1.2. This diagram shows the collision of two colliding nuclei ("Lorenz Pancakes") whose velocities are approaching the speed of light. Time is plotted along the vertical axis, where at the bottom of the diagram there is the time before the collision and at the top the time after the collision. On the horizontal axis, the position in the direction of the beam is plotted. The nuclei collided time at $t = 0$. Practically, after the collision, a fireball was created that expands in all directions and evolves in time. The fireball goes through several phases before the particles freeze out and reach the detector. Among the most important physical quantities, which describe the processes in heavy ion collisions, there are: rapidity, pseudorapidity, space-time rapidity, transverse momentum and transverse mass. When two nuclei collide, we introduce the reaction plane, which is defined by the collision parameter vector $\mathbf{b}$ and the direction of the collision. In particle physics, is commonly identified the z axis as the direction of the collision. We will call this direction *longitudinal*. *Transverse* we will call the direction perpendicular to the longitudinal and thus in the $x - y$ plane. The transverse momentum component is called *transverse momentum*

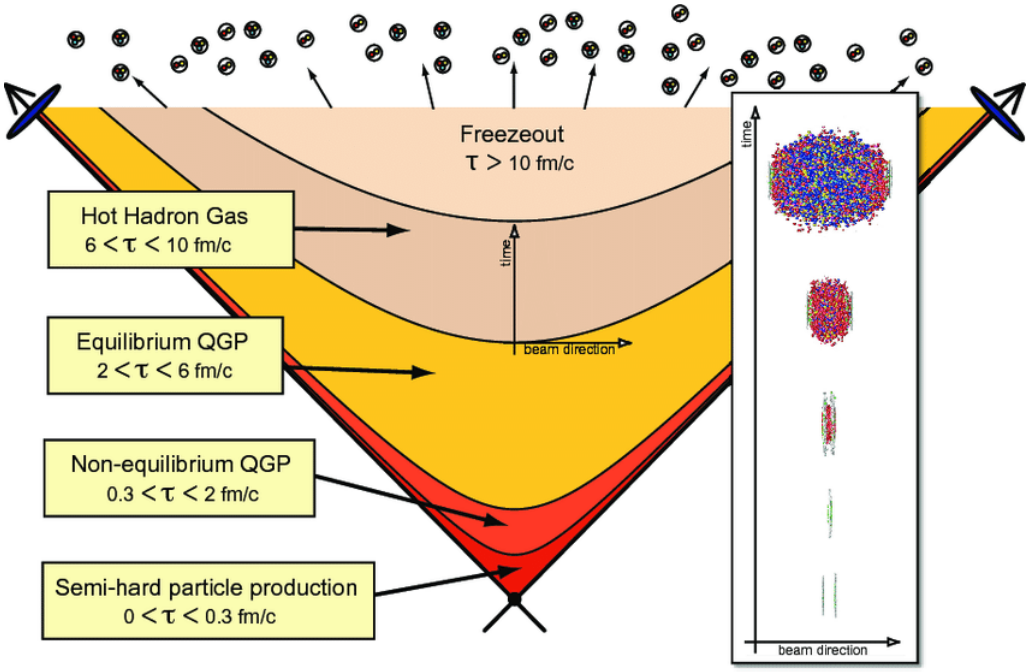

Figure 1.2: The schematic diagram of evolution of strong interacting matter, taken from [50].

p_t and is defined as

$$p_t = \sqrt{p_x^2 + p_y^2}. \tag{1.1}$$

The transverse momentum is associated with the *transverse mass*, defined as

$$m_t = \sqrt{m^2 + p_t^2}. \tag{1.2}$$

The rapidity y is a dimensionless physical quantity defined by

$$y = \frac{1}{2}\ln\left(\frac{E + p_z}{E - p_z}\right), \tag{1.3}$$

where E is the energy of the particle and p_z the z component of the four-vector of the momentum p^μ. Rapidity is a relativistic analogy of speed. If we consider a particle that is emitted with an angle θ to the collision axis, we can modify (1.3) as follows

$$y = \frac{1}{2}\ln\left(\frac{\sqrt{m^2 + p^2} + p\cos\theta}{\sqrt{m^2 + p^2} - p\cos\theta}\right). \tag{1.4}$$

For particles at very high energies, which can easily be obtained in ultra-relativistic collisions, $p \gg m$

$$y \approx \frac{1}{2}\ln\left(\frac{p + p\cos\theta}{p - p\cos\theta}\right) = -\ln\tan\frac{\theta}{2} \equiv \eta. \tag{1.5}$$

This defined quantity is called pseudorapidity η. At high energies $y \simeq \eta$. The pseudorapidity offers a great advantage. We only need the angle θ to determine it. It is also advisable to introduce the time-space rapidity η_s, which is analogical to (1.3)

$$\eta_s = \frac{1}{2}\ln\left(\frac{t + z}{t - z}\right) = \frac{1}{2}\ln\left(\frac{1 + v_z}{1 - v_z}\right), \tag{1.6}$$

where we assume a longitudinal speed in the form $v_z = \frac{z}{t}$. The evolution of a heavy ion collision can be divided into the several phases. These phases which are relevant to ultra-relativistic nuclear collisions at the RHIC or LHC accelerator.

- **PHASE I** - the initial condition of colliding nuclei
- **PHASE II** - follows just after the nuclei collide. This phase is characterised by strong gradients and large amplitude gauge fields. The duration of this phase appears to be less than 1 fm as required by hydrodynamic simulations
- **PHASE III** - a phase close to equilibrium, in which hydrodynamic description is possible. This phase lasts until the system is sufficiently diluted and enters the next phase
- **PHASE IV** - is hadronized, produces hadron gas, which is characterised by high viscosity and is described by a different equation of state than quark-gluon plasma.
- **PHASE V** - hadrons move freely from the point of collision until they decay or are captured by detectors

1.3 Anisotropic flow

The physics of the relativistic collisions of heavy ions is primarily concerned with the behaviour of dense matter and strong interaction. We want to study the collective phenomena of matter manifested in these collisions. Among such collective phenomena of quark-gluon plasma is the macroscopic flow in a particular direction. This effect should distinguish nuclear collisions from those of simpler systems, such as the proton-proton. A fireball produced in nuclear collisions can expand in the directions - the longitudinal direction and the transverse direction. The longitudinal expansion occurs for two reasons. First, the colliding nucleons (partons) of high-energy nuclei are not completely stopped by the collision and continue to move in the direction of the collision. A matter emerges between the wounded nucleons, which expands and follows their longitudinal motion. The second reason is provided by the initially conditions. The fireball will be much more contracted in the longitudinal direction than the transverse. In such a case, strong longitudinal pressure gradients arise in the fireball, forcing the whole system to expand. [14]

The expansion in a direction perpendicular to the beam is a result of interaction between the components of matter. In an extreme case, hydrodynamic behaviour is caused by the internal pressure of a highly excited matter. This is interesting because pressure is associated with energy density through the equation of state. If the pressure changes, the energy density will also change. From measuring the distribution of particles, we may be able to draw some conclusions about the pressure and the equation of state of strongly interacting matter.

In heavy ion collisions, new particles are formed and collective behaviour can be observed. Such effect is called flow, which is the result of hydrodynamic expansion

that begins just after the two nuclei collide. In this work, we will talk about 3 types of flow: **radial, elliptic, and directed**, see Figure.1.3.

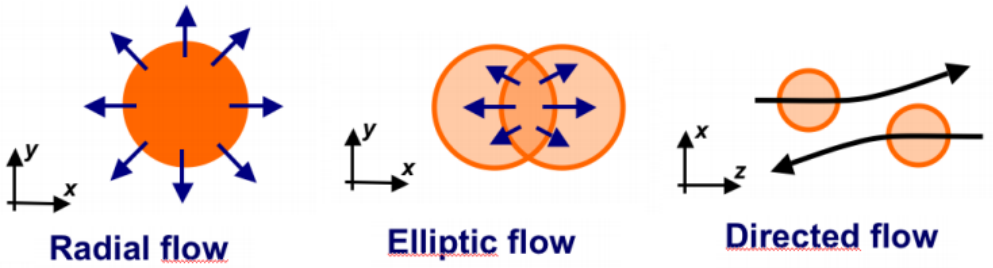

Figure 1.3: The different types of collective flow.

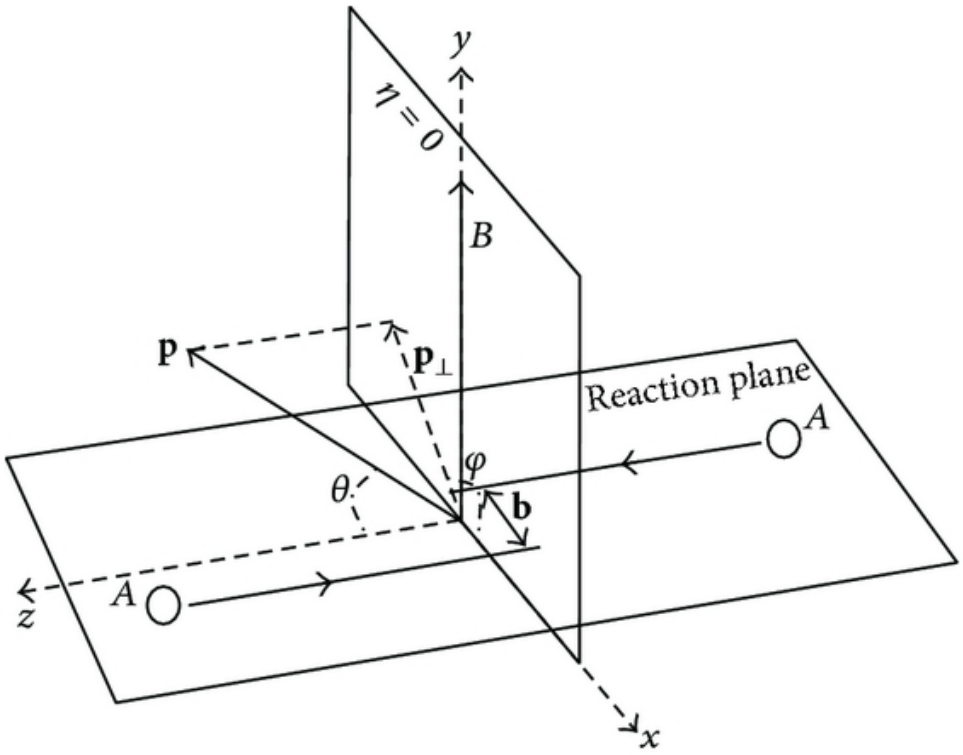

Figure 1.4: The diagram of reaction plane. Taken from [52].

In order to explain the different kinds of flow, let us first introduce several planes. The first of them is the reaction plane, which is defined by the impact parameter and the beam direction. The angle ψ_{RP} reflects the orientation of the nuclei with reference to the coordinates x, y. The reaction plane is depicted in Figure 1.4. When the existence of odd harmonics of the anisotropic flow was realised, physicists started to use the notation of participant plane ψ_{PP}, which takes into account fluctuations in the positions of nucleons inside the nuclei. However, all these "planes" are still related to the initial overlapping geometry, which cannot be measured. Flow coefficients are measured with reference to symmetry of hadron distribution plane ψ_N. Due to

fluctuations during the hydrodynamic evolution, the symmetry plane may fluctuate around the original participant plane. One more notation, which is commonly used, is an event plane ψ_{EP} which is an experimental estimation of the reaction.

Especially, we will aim on elliptic flow. Next, we can distinguish flows depending on the centrality of the collision - radial and anisotropic.

1. **Radial flow**
   We can talk about radial flow in a central collision, at a zero impact parameter of the collision. Expansion after a collision will occur in all transverse directions uniformly (isotropically), since no direction is specific from symmetry. This is an idealised situation, because even in the central collisions we do have fluctuations of the initial conditions. In other words, the initial conditions are not radial but show anisotropies. Therefore, there will be anisotropic flow also in the most central collisions

2. **Anisotropic Flow**
   The anisotropic flow occurs when the impact parameter is non-zero. So we can define the reaction plane, and there is an anisotropic production of the particles in the transverse plane. We can describe the particle distribution using the Fourier series. Consider the definition of the Fourier series of $f(x)$.

   Definition 1.3.1 *Let the f function have an absolutely convergent generalised integral (in the Riemann sense) on the interval (a, b), where $b - a = 2\pi$. Let's lay*

   $$\begin{aligned} a_n &= \frac{1}{L\pi}\int_a^b f(x)\cos\frac{n\pi x}{L}\mathrm{d}x, \\ b_n &= \frac{1}{L\pi}\int_a^b f(x)\sin\frac{n\pi x}{L}\mathrm{d}x, \forall n \in N \end{aligned} \tag{1.7}$$

   Then a trigonometric series $\frac{a_0}{2} + \sum_{n=1}^{\infty}(a_n \cos nx + b_n \sin nx)$ we call **Fourier function series f on interval** (a, b) *and the numbers a_n, b_n we call* **Fourier coefficients**.

   If we consider an even f function normalised to 1 on the $(-\pi, \pi)$ interval, then Fourier's expansion of this function will be simplified

   $$f(x) = \frac{1}{2\pi}\left(1 + 2\sum_{n=1}^{\infty} a_n \cos nx\right), \tag{1.8}$$

   where for the coefficients a_n

   $$\int_{-\pi}^{\pi} f(x)\cos(nx)\mathrm{d}x = \langle\cos(nx)\rangle_{f(x)}, \tag{1.9}$$

   where $\langle\cdots\rangle$ denotes the averaging over all the nucleons involved in the collision. For the particle momentum spectrum, we write following

   $$E\frac{\mathrm{d}^3N}{\mathrm{d}p^3} = \frac{1}{2\pi}\frac{\mathrm{d}^2N}{p_t \mathrm{d}p_T \mathrm{d}y}\left(1 + 2\sum_{n=1}^{\infty} v_n(p_t, y)\cos\left(n(\phi - \Psi_n(p_t))\right)\right), \tag{1.10}$$

where $\Psi_n(p_t)$ the angle of the symmetry plane and ϕ the angle at which the particles fly out, where the coefficients v_n apply

$$v_n(p_t, y) = \langle \cos(n(\phi - \Psi_n(p_t)) \rangle. \tag{1.11}$$

For the isotropic flow, all coefficients of v_n are equal to zero. If any of the coefficients are different from zero, they parameterise the anisotropic behaviour.

The coefficients of the anisotropic flow v_n in the measurements show dependence on centrality, transverse momentum p_t, pseudorapidity η and the type of particles. These measured dependencies can be then used primarily for determining the initial conditions of the collision, studying the transport properties of the QGP and determining the equation of state of the system.

The nuclei do not always collide head-on[1]. Hence, the expanding medium is produced with an elliptic shape and thus has non-zero elliptic spatial anisotropy ϵ_x which is defined by

$$\epsilon_x = \frac{\langle y^2 - x^2 \rangle}{\langle y^2 + x^2 \rangle}, \tag{1.12}$$

where x and y are the coordinates in the transverse plane and $\langle \cdots \rangle$ denote the averaging over energy density profile. As a consequence of the pressure gradients in different direction in the expanding fireball, the elliptic flow arise and the initial spatial anisotropy decreases. We can also define an anisotropy in the momentum space ϵ_p as

$$\epsilon_p = \frac{\langle T_{yy} - T_{xx} \rangle}{\langle T_{yy} + T_{xx} \rangle}, \tag{1.13}$$

where T_{xx} and T_{yy} are components of energy momentum tensor.

Directed flow

The directed flow is one of the key observable quantities in heavy ion collisions. Nowadays, it is defined as the first coefficient v_1 in Fourier expansion series of particle distribution. The directed flow is formed mainly in the initial phase (compression) of collisions and is therefore sensitive to early pressure gradients in the evolving nuclear matter. So the directed flow begins by examining the rigidity of the nuclear equation of state, which is of major interest to heavy ion research and astrophysics. Because of symmetry, we have no directional flow at $y = 0$. The behaviour of directed flow for protons is depicted in Figure 1.5. There is a comparison of hydrodynamic simulation Glissando+vHLLE at $\sqrt{s_{NN}} = 27$ GeV and experimental data from STAR experiment.

[1] impact parameter is zero

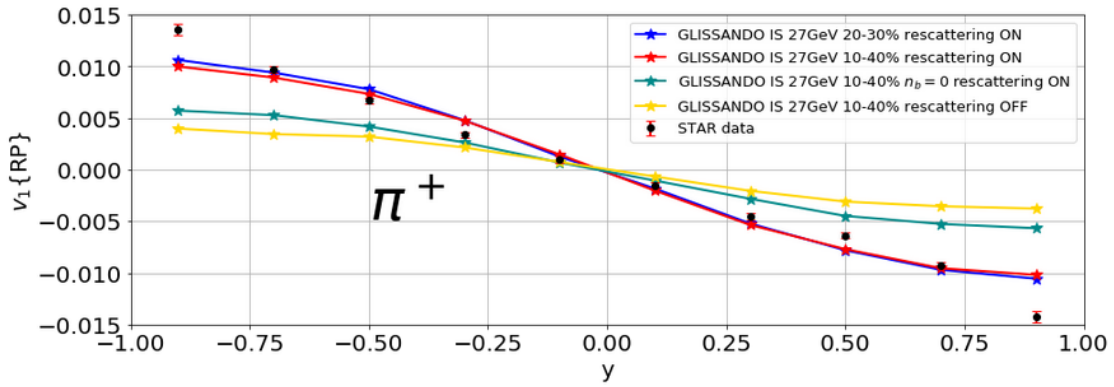

Figure 1.5: The directed flow $v_1(y)$ for pions in Au+Au collisions at $\sqrt{s_{NN}} = 27$ GeV for centralities 10-40% and 20-30% from vHLLE + UrQMD simulations with GLISSANDO [42]. Experimental data taken from [11].

Elliptic flow

The elliptic flow is defined as the second order coefficient v_2 in Fourier's expansion series of particle distribution. It has been shown that the value of the v_2 coefficient increases with increasing p_T. If the p_T is equal to zero, v_2 is, necessarily, zero. This behaviour is because of the symmetry. The elliptic flow strongly depends on centrality. The elliptic flow increases with increasing centrality, which is depicted in Figure. 1.6. This figure is only illustrative.

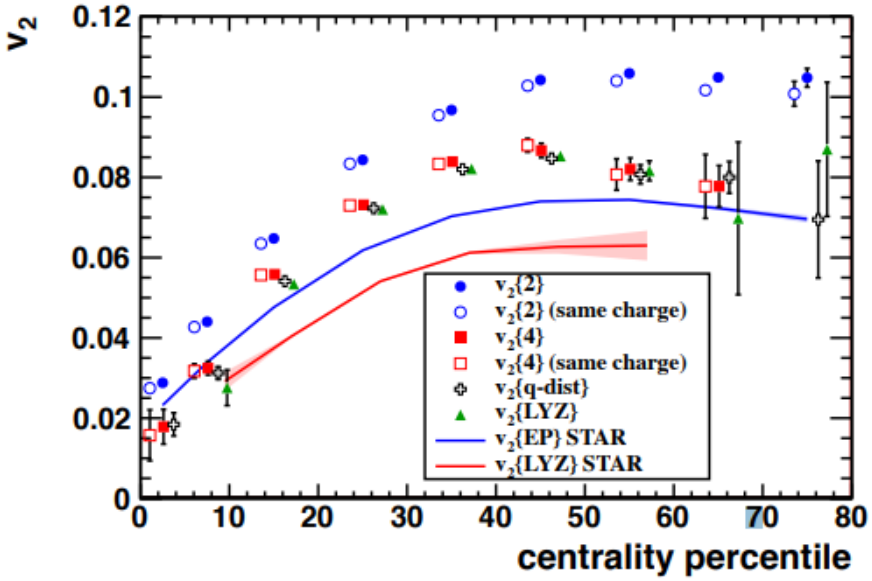

Figure 1.6: Elliptic flow integrated over the pt range $0.2 < p_t < 5.0$ GeV/c, as a function of event centrality, for the 2- and 4-particle cumulant methods, a fit of the distribution of the flow vector, and the Lee-Yang Zeroes method. Data points are form RHIC measurements for Au–Au at $\sqrt{s_{nn}} = 200$ GeV. Taken from [2].

1.3.1 Methods of flow measurement

There exists several method how to obtain flow from measured data. In the following sub-chapter we will describe two common methods: the event plane method and the comulant method.

1.3.2 Event plane method

The first method how to compute flow is the *event plane method* [39]. In practice, the reaction plane can not be found but it can only be approximated and this approximated reaction plane is known as event plane. The event flow vector Q_n and event plane angle Ψ_{RP} from the $n-th$ harmonics are defined as

$$\begin{aligned} Q_n \sin(n\Psi_{RP}) = Y_n &= \sum_i w_i \sin(n\phi_i), \\ Q_n \cos(n\Psi_{RP}) = X_n &= \sum_i w_i \cos(n\phi_i), \\ \Psi_{RP} &= \frac{\arctan \frac{\sum_i w_i \sin(n\phi_i)}{\sum_i w_i \cos(n\phi_i)}}{n}, \end{aligned} \tag{1.14}$$

where w_i are weights and ϕ_n is particle's azimuthal angle. The summation in (1.14) goes over all particles of an event. Then the observable flow is computed as

$$v_n = \langle \cos(n(\phi - \Psi_{RP})) \rangle, \tag{1.15}$$

and flow fluctuation are given then

$$\mathrm{Var}(v_n) \equiv \langle v_n^2 \rangle - \langle v_n \rangle^2, \tag{1.16}$$

where $\langle \cdots \rangle$ denotes averaging over event and

$$\begin{aligned} \langle v_n^2 \rangle &= \langle \cos(n(\phi - \Psi_{RP}))^2 \rangle \\ \langle v_n \rangle^2 &= \langle \cos(n(\phi - \psi_{RP})) \rangle^2. \end{aligned} \tag{1.17}$$

We will often use the symbol $\delta v_n \equiv \sqrt{\mathrm{Var}(v_n)}$ [39]. In this work sections, we will focus our attention on the second harmonics the v_2.

1.3.3 Cumulant method

The second method, which will be discussed is cumulant method [12, 16, 20]. The symmetry plane can not be exactly measured experimentally. The event-plane method estimates the symmetry plane. However, this method strongly depends on the detector resolution, and gives inaccurate results. Instead, we measure two-particle (and many-particle) correlations. The two-particle *cumulants* of the v_n for the two particle correlation function is given as

$$\begin{aligned} c_n\{2\} &= \langle \langle e^{i[n(\phi_1 - \phi_2)]} \rangle \rangle = \langle \langle e^{i[n(\phi_1 - \phi_2 - \Psi_m + \Psi_m)]} \rangle \rangle \\ &= \langle \langle e^{i[n(\phi_1 - \Psi_m)]} \rangle \langle e^{-i[n(\phi_2 - \Psi_m)]} \rangle + \delta_2 \rangle \\ &= \langle v_n^2 + \delta_2 \rangle. \end{aligned} \tag{1.18}$$

For four-particle cumulants, we obtain

$$\begin{aligned} c_n\{4\} &= \langle\langle e^{i[n(\phi_1+\phi_2-\phi_3-\phi_4)]}\rangle\rangle - 2\langle\langle e^{i[n(\phi_1-\phi_2)]}\rangle\rangle^2 \\ &= \langle -v_n^4 + \delta_4 + 4v_n^2\delta_2 + 2\delta_2^2\rangle - 2\langle v_n^2 + \delta_2\rangle^2 \\ &= \langle -v_n^4 + \delta_4\rangle. \end{aligned} \tag{1.19}$$

By the delta, in these expressions, the $non - flow$ effects are included such as jets and resonance decays. Non-flow effects tend to artificially increase the signal of flow. [16]

1.3.4 Flow angle and magnitude fluctuations in heavy ion collision

In this section we present both theoretical and experimental descriptions of flow fluctuations in heavy ion collisions. The initial anisotropies of the colliding nuclei and energy density inhomogeneities drive the collective expansion of the QGP, which ultimately results in a momentum anisotropy in the final state. This momentum anisotropy is characterized by Fourier expansion of the distribution of azimuthal angles of the emitted particles (1.10).

The largest flow coefficient, elliptic flow v_2, is determined by the geometrical overlap of nuclei colliding at a finite impact parameter b. Fluctuations in the position of colliding nuclei and nucleons within the nuclei can induce more complex geometrical shapes, leading to nonzero flow coefficients with $n > 2$, such as triangular flow v_3. These coefficients have been measured extensively at RHIC and the LHC, and comparisons of measurements with hydrodynamical calculations have been used to constrain initial conditions and transport properties of the QGP.

The p_t-dependent flow vector fluctuations are studied with p_t-differential flow coefficients. The regular p_t-differential flow coefficient is defined as

$$v_n\{2\} = \frac{\langle\langle \cos n(\varphi_1^{POI} - \varphi_1)\rangle\rangle}{\sqrt{\langle\langle \cos n(\varphi_1 - \varphi_2)\rangle\rangle}}, \tag{1.20}$$

where φ_1^{POI} represents the azimuthal angle of a specific particle of interest (POI) that is selected from a narrow p_t range, while φ denotes the azimuthal angle of a reference particle (RP) that has been chosen from a wide p_t range. The single bracket notation indicates an average taken over all events, while the double bracket notation indicates an average taken over all particles and all events. The $v_2\{2\}$ observable is used to probe the p_t-differential flow, which is sensitive to both the magnitude and angle fluctuations of the flow. Another p_t-differential flow which is unaffected by the flow vector fluctuations

$$v_n[2] = \sqrt{\langle\langle \cos n(\varphi_1^{POI} - \varphi_2^{POI})\rangle\rangle} = \sqrt{\langle v_n^2(p_t)\rangle}, \tag{1.21}$$

since $v_n[2]$ is not affected by the flow angle and flow magnitude fluctuation.

Previous equations rely on observables constructed from two-particle correlations, which could not separate flow angle and magnitude fluctuations. A new four-particle

correlation functions discussed in [40, 41] can separate p_T-dependent fluctuations of the flow angle and flow magnitude. Flow angle fluctuations can be quantified by

$$A_f^n = \frac{\langle\langle\cos[\varphi_1^a + \varphi_2^a - \varphi_3 - \varphi_4]\rangle\rangle}{\langle\langle\cos[\varphi_1^a + \varphi_2 - \varphi_3^a - \varphi_4]\rangle\rangle} = \frac{\langle v_n^2(p_t^a)v_n^2\cos 2n[\phi_n(p_t^a) - \psi_n]]\rangle}{\langle v_n^2(p_t^a)v_n^2\rangle} \approx \\ \approx \langle\cos 2n[\phi_n(p_t^a) - \psi_n]]\rangle_w, \tag{1.22}$$

where a represents an associated particle that has been selected from a narrow transverse momentum range, denoted as p_t^a, w indicates that the quantity has been averaged over all events, where each event is weighted by the fourth power of v_n. A value of $A_f^n < 1$ suggests the existence of flow angle fluctuations that are dependent on p_t. The degree of deviation from unity indicates the level of correlation between the symmetry plane at a specific p_t and the common symmetry plane. The magnitude of the flow is determined by the double ratio of the p_t-differential flow fluctuations

$$M_f^n = \frac{\langle\langle\cos[\varphi_1^a + \varphi_2 - \varphi_3^a - \varphi_4]\rangle\rangle/(\langle\langle\cos n(\varphi_1^a - \varphi_3^a)\rangle\rangle\langle\langle\cos n(\varphi_2 - \varphi_4)\rangle\rangle)}{\langle\langle\cos[\varphi_1 + \varphi_2 - \varphi_3 - \varphi_4]\rangle\rangle/\langle\langle\cos n(\varphi_1 - \varphi_2)\rangle\rangle^2}. \tag{1.23}$$

A deviation M_f^n from unity indicates the presence of p_t-dependent flow magnitude fluctuations. The magnitude of the deviation will show how strongly the flow magnitude is decorrelated at a specific p_t range with respect to the integrated flow. These new correlators probe a higher moment of the distribution of flow fluctuations compared to correlators traditionally used in studies of flow and flow fluctuations using two-particle techniques.

At this point, it is really challenging and difficult to directly calculate the equations (1.22) and (1.23). In the high energy physics, especially at LHC and RHIC energies, the anisotropic flow observables are commonly computed using the two- and multi-particle correlation method [12, 20]. This method involves studying the correlation functions between particles, and the Generic Framework [17, 27]. This framework allows for a rapid and accurate computation of multi-particle correlations. However, to separate the flow angle and flow magnitude fluctuations, additional correlators must be added into the Generic Framework, as described in equations (1.22) and (1.23). The anisotropic flow correlations are expressed in terms of the Q-vector

$$Q_{n,p} = \sum_{k=1}^{M} w_k^p e^{in\varphi_k}, \tag{1.24}$$

where M is the total number of the particles in a given kinematic range, φ is the azimuthal angle of the particles, and w is a particle weight. In general, the single-event m-particle correlation can be calculated with

$$\langle m_{n_1,\ldots,n_m}\rangle = \frac{\sum_{k_1\neq\ldots\neq k_m}^{M} w_{k_1}^p \ldots . w_{k_m}^p e^{i(n_1\varphi_1+\ldots+n_m\varphi_m)}}{\sum_{k_1\neq\ldots\neq k_m}^{M} w_{k_1}^p \ldots . w_{k_m}^p}, \tag{1.25}$$

The numerator and denominator in (1.25) are trivially related via equations

$$\begin{aligned} N\langle m\rangle_{n_1,\ldots,n_m} &= \sum_{k_1\neq\ldots\neq k_m}^{M} w_{k_1}^p \ldots . w_{k_m}^p e^{i(n_1\varphi_1+\ldots+n_m\varphi_m)}, \\ D\langle m\rangle_{n_1,\ldots,n_m} &= \sum_{k_1\neq\ldots\neq k_m}^{M} w_{k_1}^p \ldots . w_{k_m}^p = N\langle m\rangle_{0,..,0}. \end{aligned} \tag{1.26}$$

The event-average of two- and four-particle correlations can then be obtained with [17, 27]

$$\begin{aligned}\langle\langle 2\rangle\rangle &= \frac{\sum_{events} N\langle 2\rangle_{n_1,n_2}}{\sum_{events} D\langle 2\rangle_{n_1,n_2}},\\ \langle\langle 4\rangle\rangle &= \frac{\sum_{events} N\langle 4\rangle_{n_1,n_2,n_3,n_4}}{\sum_{events} D\langle 4\rangle_{n_1,n_2,n_3,n_4}}\end{aligned} \tag{1.27}$$

where the double brackets refer to an average over all particles and events. For p_t-differential anisotropic flow, one or more of the particles are selected from a narrow p_t range by constructing a p-vector analogous to the Q-vector consisting only of POI [40]

$$p_{n,p} = \sum_{k=1}^{M_{POI}} w_k^p e^{in\varphi_k}, \tag{1.28}$$

where M_{POI} is the number of the POIs in the selected kinematic region. The p-vector enables the calculation of various p_t-differential anisotropic flow coefficients, such as $v_n\{2\}$ by selecting one POI and one RP or $v_n[2]$ by selecting two POIs. Additionally, the double-differential two-particle correlations are calculated with one associate particle and one trigger particle from different narrow p_T-ranges. The p_t-differential two-particle correlations are [40]

$$\begin{aligned}N\langle 2'\rangle_{n_1,n_2} &= Q_{n_1,1}p_{n_2,1} - q_{n_1+n_2,2},\\ N\langle 2''\rangle_{n_1,n_2} &= p_{n_1,1}p_{n_2,1} - p_{n_1+n_2,2},\end{aligned} \tag{1.29}$$

where $q_{n,p}$ is the overlap-vector of particles that are both POIs and RPs. The event-averaged p_t-differential correlations then

$$\begin{aligned}\langle\langle 2'\rangle\rangle &= \frac{\sum_{events} N\langle 2''\rangle_{n_1,n_2}}{\sum_{events} D\langle 2'\rangle_{n_1,n_2}},\\ \langle\langle 2''\rangle\rangle &= \frac{\sum_{events} N\langle 2''\rangle_{n_1,n_2}}{\sum_{events} D\langle 2''\rangle_{n_1,n_2}}.\end{aligned} \tag{1.30}$$

Non-flow effects are correlations not due to collective effects, such as resonance decays and jets. They can be suppressed by applying a gap in pseudorapidity, $|\Delta\eta|$, between two subevents, A and B, from which the particles are selected.

$$\begin{aligned}N\langle 2\rangle^{|\Delta\eta|}_{n_1,n_2} &= Q^A_{n_1,1}Q^B_{n_2,1},\\ N\langle 4\rangle^{|\Delta\eta|}_{n_1,n_2,n_3,n_4} &= N\langle 2\rangle^A_{n_1,n_2}N\langle 2\rangle^B_{n_1,n_2},\end{aligned} \tag{1.31}$$

For p_t-differential correlators the subevents are implemented

$$\begin{aligned}N\langle 2'\rangle^{|\Delta\eta|}_{n_1,n_2} &= p^A_{n_1,1}Q^B_{n_2,1},\\ N\langle 2''\rangle^{|\Delta\eta|}_{n_1,n_2} &= p^A_{n_1,1}p^B_{n_2,1},\end{aligned} \tag{1.32}$$

To compute equations (1.23) and (1.23), four-particle correlations are necessary, and these are obtained through the subevent method to minimize any potential non-flow contamination. When studying four-particle correlations with a pseudorapidity gap, there is a decision to be made regarding how to group the particles of interest

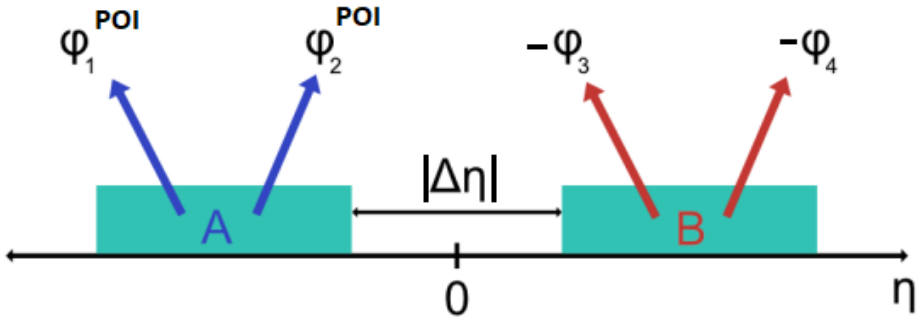

Figure 1.7: The event divided into two subevents separated by a gap in pseudorapidity.

(POIs) and reference particles (RPs). One option is to select the POIs from the same subevents (SS), while the other approach involves selecting one POI from opposite subevents (OS), as depicted in Fig 1.7. The equation for four-particle correlations are then

$$\begin{aligned} N\langle 4'\rangle_{SS} &= (p_{n_1,1}p_{n_2,1} - p_{n_1+n_2,2})^A (Q_{n_3,1}Q_{n_4,1} - Q_{n_3+n_4,2})^B, \\ N\langle 4'\rangle_{OS} &= (p_{n_1,1}Q_{n_2,1} - q_{n_1+n_2,2})^A (p_{n_3,1}Q_{n_4,1} - q_{n_3+n_4,2})^B. \end{aligned} \tag{1.33}$$

The four-particle correlations are, by construction, less sensitive to non-flow correlations. The p_t-differential flow coefficient $v_2\{2\}$ is

$$v_2\{2\} = \frac{\langle\langle 2'\rangle\rangle}{\sqrt{\langle\langle 2\rangle\rangle}}, \tag{1.34}$$

and the alternative p_t-differential flow coefficient $v_n[2]$ becomes

$$v_n[2] = \sqrt{\langle\langle 2''\rangle\rangle}. \tag{1.35}$$

Finally, the observables based on four-particle correlations, A_n^f and M_n^f, which describe the flow angle and flow magnitude fluctuations, respectively, are given by

$$\begin{aligned} A_n^f &= \frac{\langle\langle 4'\rangle\rangle_{SS}}{\langle\langle 4'\rangle\rangle_{OS}}, \\ M_n^f &= \frac{\langle\langle 4'\rangle\rangle_{OS}/(\langle\langle 2''\rangle\rangle\langle\langle 2\rangle\rangle)}{\langle\langle 4\rangle\rangle/\langle\langle 2\rangle\rangle^2}. \end{aligned} \tag{1.36}$$

The A_2^f measurements as a function of the associate particle transverse momentum p_t^a in centrality classes 0–5%, 10–20%, and 30–40% are shown in Fig 1.8. The increasing deviation from unity with p_t^a above 3 GeV/c observed in data suggests that the elliptic flow at large transverse momentum ($p_t > 2.5$ GeV/c) may not be correlated with a common symmetry plane. Theoretical calculations from iEBE-VISHNU [46], MUSIC [33, 45] as well as AMPT [34, 36] models are, when available, compared to the data in Fig. 1.8. The iEBE-VISHNU model is a (2+1)D viscous hydrodynamical model coupled to the hadronic cascade model UrQMD [19].

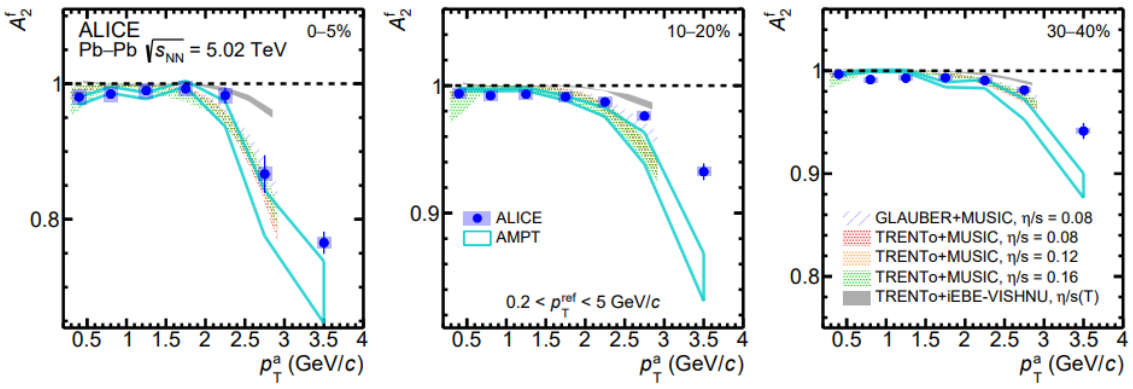

Figure 1.8: The flow angle fluctuation A_2^f in Pb–Pb collisions at $\sqrt{s_{NN}} = 5.02$ TeV as a function of the associate particle transverse momentum p_t^a in centrality classes 0–5% (left), 10–20% (middle), and 30–40% (right). Comparison with iEBE-VISHNU with TRENTo initial conditions and $\eta/s(T)$ [54], iEBE-VISHNU with AMPT initial conditions and $\eta/s = 0.08$ [54] and $\eta/s = 0.20$, CoLBT [55], and AMPT [36] are shown as coloured bands. Taken from [41].

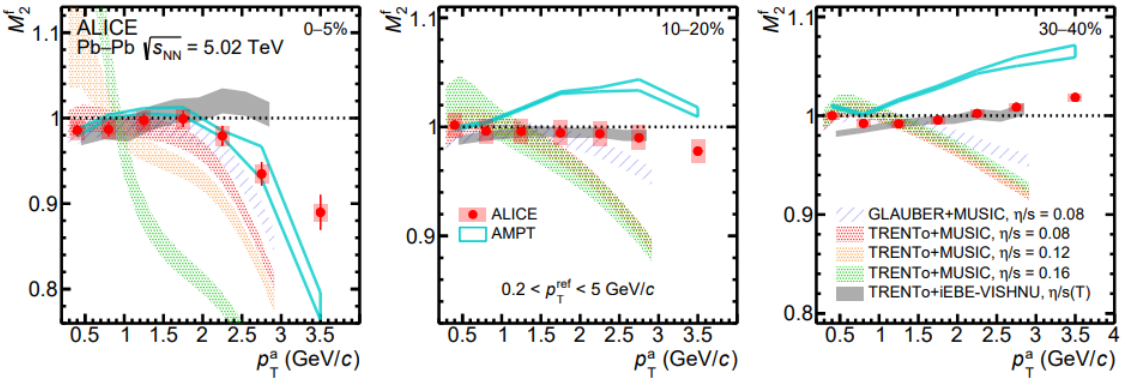

Figure 1.9: The flow magnitude fluctuation M_2^f in Pb–Pb collisions at $\sqrt{s_{NN}} = 5.02$ TeV as a function of the associate particle transverse momentum p_t^a in centrality classes 0–5% (left), 10–20% (middle), and 30–40% (right). Comparison with iEBE-VISHNU with TRENTo initial conditions and $\eta/s(T)$ [54], MUSIC with Glauber initial conditions and $\eta/s = 0.08$ [88], MUSIC with TRENTo initial conditions and $\eta/s = 0.08, 0.12, 0.16$ [21], and AMPT [36] are shown as coloured bands. Taken from [41].

The measurements of the p_t-dependent fluctuations of the flow magnitude M_2^f, as a function of the associate particle transverse momentum p_t^a in centrality classes 0–5%, 10–20%, and 30–40% are shown in Fig 1.9.

Chapter 2

Relativistic hydrodynamics

The physical description of a system consisting of many degrees of freedom is generally a challenging and non-trivial task. The mathematical formulation of a theory, which describes the microscopic dynamics of a system containing a large number of interacting particles is one of the most challenging problems in theoretical physics. Nevertheless, there exists possibility to provide an effective macroscopic description which takes into account the degrees of freedom relevant on long time scales. Most microscopic variables fluctuate rapidly in space and time, therefore only the average values of quantities like energy and momentum density can be observed on macroscopic scales. Hydrodynamics is one of the most common examples of such a situation.

The relativistic hydrodynamics is very interesting theory, because it is simple and general. The simplicity comes from the fact, that the information about the system is comprised in its thermodynamic properties, the equation of state, and the initial conditions. The hydrodynamics is also general in the sense that it is based on the assumption that we can neglect the microscopic length scales relative to the length scale of the whole system. A further assumption regarding the nature of particles and their interactions, classical/quantum phenomena is not made. This simplicity is the foundation of the applicability of hydrodynamic description in heavy ion collisions. [43]

In the next chapter, we summarise the basic mathematical apparatus that is used to derive relativistic hydrodynamic equations.

2.1 Energy and momentum tensor

For a system described by the Lagrangian density $\mathcal{L}$, the equations of motion take the form

$$\frac{\partial}{\partial x^\mu}\left(\frac{\partial \mathcal{L}}{\partial q_{a,\mu}}\right) - \frac{\partial \mathcal{L}}{\partial q_a} = 0, \tag{2.1}$$

where a, q_a denotes the general coordinate, $q_{a,\mu} \equiv \frac{\partial q_a}{\partial x^\mu}$. From Noether's theorem, we know that every continuous one-parameter group of transformations that leaves

the action $S = \frac{1}{c}\int_{V^*} \mathcal{L} \mathrm{d}V^*$ invariant, where V^* is volume of space, belongs to the four-vector k^μ satisfying $\frac{\partial k^\mu}{\partial x^\mu} = 0$, so called conserved the four-current. [48, 49] Consider a transformation as a translation of $\tilde{x}^\mu = x^\mu + b^\mu$, in which field variables are transformed by $\tilde{q}_a(\tilde{x}) = q_a(x)$. The density of the Lagrange function $\mathcal{L}$ will be invariant to the translation, if it does not explicitly depend on the coordinates x^μ, or $\mathcal{L}(\tilde{q}_a, \tilde{q}_{a,\mu}) = \mathcal{L}(q_a, q_{a,\mu})$. This can be expressed by vanishing derivative of $\mathcal{L}$ according to x^μ

$$0 = \left(\frac{\partial \mathcal{L}}{\partial x^\mu}\right)_{expl} = \frac{\partial \mathcal{L}}{\partial x^\mu} - \frac{\partial \mathcal{L}}{\partial q_a} q_{a,\mu} - \frac{\partial \mathcal{L}}{\partial q_{a,\nu}} q_{a,\nu\mu}. \tag{2.2}$$

Hence, using the equations of motion (2.1)

$$0 = \delta^\mu_\nu \frac{\partial}{\partial x^\nu} - \frac{\partial}{\partial x^\nu}\left(\frac{\partial \mathcal{L}}{\partial q_{a,\nu}}\right) - \frac{\partial \mathcal{L}}{\partial q_{a,\nu}} q_{a,\nu\mu} = \frac{\partial}{\partial x^\nu}\left(\frac{\partial \mathcal{L}}{\partial q_{a,\nu}} q_{a,\mu} - \delta^\mu_\nu \mathcal{L}\right). \tag{2.3}$$

For $\mu = 0, 1, 2, 3$, the equations represent the laws of conservation of energy (for $\nu = 0$) and momentum (for $\nu = 1, 2, 3$) in field theory. Let us now define the tensor of energy and momentum

$$T^\nu_\mu \equiv \frac{\partial \mathcal{L}}{\partial q_{a,\nu}} q_{a,\mu} - \delta^\mu_\nu \mathcal{L}, \tag{2.4}$$

In addition, the tensor thus defined is symmetric $T^{\mu\nu} = T^{\nu\mu}$, and must satisfy the equations of motion (2.3)

$$\frac{\partial}{\partial x^\mu} T^\nu_\mu = 0, \text{ or } \frac{\partial}{\partial x^\mu} T^{\mu\nu} = 0. \tag{2.5}$$

If we mark $\frac{\partial}{\partial x^\mu} \equiv \partial_\mu$, then the above relationship takes the form: $\partial_\mu T^{\mu\nu} = 0$. This derivation of the tensor of energy and momentum has one disadvantage. This derivation of (2.5) is in Minkowski spacetime, which does not include the case of the general curved coordinates. Our goal is to convert the equations (2.5) into a covariant form in which all the components are transformed in the same way. For this purpose, we introduce *covariant derivative* in the next chapter.

2.2 Coordinate Transformation

The basic postulate of relativity is the principle of covariance, which tells us that in all systems the laws of physics are same and the speed of light is constant [48]. All events occurring in spacetime are represented by points. In mathematical terms, it is a four-dimensional manifold with the metric tensor $g_{\mu\nu}$ so that the length element between two points is equaled

$$\mathrm{d}s^2 = g_{\mu\nu} \mathrm{d}x^\mu \mathrm{d}x^\nu. \tag{2.6}$$

The length element size is the same for all observers, when coordinates change $\tilde{x}^\mu = \tilde{x^\mu}(x^\alpha)$

$$\mathrm{d}s^2 = \tilde{g}_{\mu\nu} \mathrm{d}\tilde{x}^\mu \mathrm{d}\tilde{x}^\nu = g_{\alpha\beta} \mathrm{d}x^\alpha \mathrm{d}x^\beta = g_{\alpha\beta} \frac{\partial x^\alpha}{\partial \tilde{x}^\mu} \frac{\partial x^\beta}{\partial \tilde{x}^\nu} \mathrm{d}x^\mu \mathrm{d}x^\nu. \tag{2.7}$$

By comparing the terms of the equation (2.7), we get the transformation for the metric tensor

$$\tilde{g}_{\mu\nu} = g_{\alpha\beta}\frac{\partial x^{\alpha}}{\partial \tilde{x}^{\mu}}\frac{\partial x^{\beta}}{\partial \tilde{x}^{\nu}}. \tag{2.8}$$

At the same time, the inverse tensor k $g_{\mu\nu}$ is $g^{\mu\nu}$, so that: $g_{\mu\nu}g^{\nu\rho} = \delta^{\rho}_{\mu}$.

2.3 Covariant derivative

Consider a vector space $\mathcal{V}$ with base vectors $\mathbf{e}_{\mu} = \mathbf{e}_{\mu}(\mathbf{x})$, where $\mathbf{x}$ are general coordinates, base vectors are dependent on general coordinates, and the derivative of $\mathbf{v}$

$$\partial_{\mu}\mathbf{v} = \partial_{\mu}(v^{\nu}\mathbf{e}_{\nu}) = (\partial_{\mu}v^{\nu})\,\mathbf{e}_{\nu} + v^{\nu}\,(\partial_{\mu}\mathbf{e}_{\nu})\,. \tag{2.9}$$

The part $\partial_{\mu}v^{\nu}$ expresses the change of the vector in the component v^{ν}, the second term $\partial_{\mu}\mathbf{e}_{\nu}$ expresses the change of the base vector, which is caused, for example, by the choice of curved coordinates. For linear coordinates, the second term is equal to zero, $\partial_{\mu}\mathbf{e}_{\nu} = 0$. Let us now define Christoffel symbols as

$$\partial_{\mu}\mathbf{e}_{\nu} \equiv \Gamma^{\lambda}_{\nu\mu}\mathbf{e}_{\lambda}. \tag{2.10}$$

Christofell symbols carry information about the change of the metric tensor from point to point in the space-time. [43]. By changing $\nu \leftrightarrow \lambda$ we rewrite (2.9)

$$\partial_{\mu}\mathbf{v} = (\partial_{\mu}v^{\nu} + v^{\lambda}\Gamma^{\nu}_{\lambda\mu})\mathbf{e}_{\nu}. \tag{2.11}$$

The expression in parentheses (2.11) is called *covariant derivative*, the first part of the derivative is an ordinary partial derivative and the second part is caused by curvy coordinates [49]. The covariant derivative is denoted by ∇_{μ}. From the equation (2.11), we see that the covariant derivative acts on the vector by components

$$\nabla_{\mu}v^{\nu} = \partial_{\mu}v^{\nu} + v^{\lambda}\Gamma^{\nu}_{\lambda\mu}. \tag{2.12}$$

The equation (2.10) is not very useful for calculating Christoffel symbols, because we do not yet know how to calculate $v^{\lambda}\Gamma^{\nu}_{\lambda\mu}e_{\nu}$ at each point of space. In fact, Christoffel's symbols are related to the metric tensor $g_{\mu\nu}$. Consider the metric tensor $g_{\mu\nu} = \mathbf{e}_{\mu}\mathbf{e}_{\nu}$, where $\mathbf{e}_{\mu}$ and $\mathbf{e}_{\nu}$ are the base vectors. Now we take the derivative of $g_{\mu\nu}$ with respect to x^{λ}

$$\begin{aligned}\frac{\partial g_{\mu\nu}}{\partial x^{\lambda}} &= \frac{\partial\left(\mathbf{e}_{\mu}\mathbf{e}_{\nu}\right)}{\partial x^{\lambda}} = \left(\frac{\partial \mathbf{e}_{\mu}}{\partial x^{\lambda}}\right)\mathbf{e}_{\nu} + \mathbf{e}_{\mu}\left(\frac{\partial \mathbf{e}_{\nu}}{\partial x^{\lambda}}\right),\\ &= \Gamma^{\rho}_{\lambda\mu}\mathbf{e}_{\rho}\mathbf{e}_{\nu} + \Gamma^{\rho}_{\lambda\nu}\mathbf{e}_{\rho}\mathbf{e}_{\mu},\\ &= \Gamma^{\rho}_{\lambda\mu}g_{\rho\nu} + \Gamma^{\rho}_{\lambda\nu}g_{\rho\mu}.\end{aligned} \tag{2.13}$$

Now let us permute the indices μ, ν and λ and create combinations

$$\frac{\partial g_{\mu\nu}}{\partial x^{\lambda}} = g_{\rho\nu}\Gamma^{\rho}_{\lambda\mu} + g_{\rho\mu}\Gamma^{\rho}_{\lambda\nu}, \tag{2.14}$$

$$\frac{\partial g_{\lambda\nu}}{\partial x^{\mu}} = g_{\rho\nu}\Gamma^{\rho}_{\mu\lambda} + g_{\rho\lambda}\Gamma^{\rho}_{\mu\nu}, \tag{2.15}$$

$$-\frac{\partial g_{\mu\lambda}}{\partial x^{\nu}} = -g_{\rho\lambda}\Gamma^{\rho}_{\nu\mu} - g_{\rho\mu}\Gamma^{\rho}_{\nu\lambda}, \tag{2.16}$$

Since Christoffel symbols are symmetric relative to the subscripts $\Gamma^{\rho}_{\nu\mu} = \Gamma^{\rho}_{\mu\nu}$ and after adding the above equations we get

$$2g_{\rho\nu}\Gamma^{\rho}_{\mu\lambda} = \left[\frac{\partial g_{\mu\nu}}{\partial x^{\lambda}} + \frac{\partial g_{\lambda\nu}}{\partial x^{\mu}} - \frac{\partial g_{\mu\lambda}}{\partial x^{\nu}}\right], \tag{2.17}$$

We multiply this equation by $g^{\sigma\nu}$ and use the knowledge that $g^{\sigma\nu}g_{\rho\nu} = \delta^{\sigma}_{\rho}$ [43]. We get the formula for the Christoffel symbols from the metric

$$\Gamma^{\sigma}_{\mu\lambda} = \frac{1}{2}g^{\sigma\nu}\left[\frac{\partial g_{\mu\nu}}{\partial x^{\lambda}} + \frac{\partial g_{\lambda\nu}}{\partial x^{\mu}} - \frac{\partial g_{\mu\lambda}}{\partial x^{\nu}}\right]. \tag{2.18}$$

The covariant derivative can be generalized to the general tensor $T^{\mu_1\dots\mu_p}_{\nu_1\dots\nu_q}$ of type $\binom{p}{q}$ (the contravariant order p and the covariant order q)

$$\begin{aligned}\nabla_{\lambda}T^{\mu_1\dots\mu_p}_{\nu_1\dots\nu_q} = \partial_{\lambda}T^{\mu_1\dots\mu_p}_{\nu_1\dots\nu_q} + \Gamma^{\mu_1}_{\lambda\alpha}T^{\alpha\mu_2\dots\mu_p}_{\nu_1\dots\nu_q} + \dots + \Gamma^{\mu_p}_{\lambda\alpha}T^{\mu_1\mu_2\dots\alpha}_{\nu_1\dots\nu_q} - \\ -\Gamma^{\alpha}_{\lambda\nu_1}T^{\nu_1\mu_2\dots\mu_p} - \alpha\nu_2\dots\nu_q - \dots - \Gamma^{\alpha}_{\lambda\nu_q}T^{\nu_1\mu_2\dots\mu_p}_{\nu_1\nu_2\dots\alpha}.\end{aligned} \tag{2.19}$$

As we have already mentioned, the relativistic formulation of hydrodynamics must satisfy the basic principle of covariance. Then let us rewrite the relationship (2.5) into a covariant form

$$\nabla_{\mu}T^{\mu\nu} = 0. \tag{2.20}$$

2.4 Relativistic kinetic theory

In this chapter we introduce the interpretation of basic objects, which we then use in hydrodynamics. As in the non-relativistic case, the basic local particle density function $n(\mathbf{x}, t)$ is constructed as $n(\mathbf{x}, t)\mathrm{d}^3x$, which gives the number of particles in the spatial volume d^3x around the point $\mathbf{x}$ at the time t [13]. Similarly, we define the particle flow of $\mathbf{j}(x, t)$. In relativity, these variables form the components of a four-vector

$$N^{\mu}(x) = (n(x^{\mu}, t), \mathbf{j}(x^{\mu}, t)), \tag{2.21}$$

where $x^{\mu} = (t, \mathbf{x})$ is a spacetime point. Now we describe the particle on its *hypersurface*. This simply means that the norm of their four-momentum is equal to the square of the mass

$$p^{\mu}g_{\mu\nu}p^{\nu} = (p^0)^2 - \mathbf{p}^2 = m^2. \tag{2.22}$$

For a large number of particles, it makes sense to introduce *particle distribution in phase space* $f(x, p)$ so that $f(x, p)\mathrm{d}^3\mathbf{x}\mathrm{d}^3\mathbf{p}$ indicates the number of particles in the phase space volume element $\mathrm{d}^3\mathbf{x}\mathrm{d}^3\mathbf{p}$ around the point $(\mathbf{x}, \mathbf{p})$ at time t. Then we are able to define local density and current as

$$\begin{aligned}n(\mathbf{x}, t) &= \int \mathrm{d}^3\mathbf{p}f(x, p), \\ \mathbf{j}(\mathbf{x}, t) &= \int \mathrm{d}^3\mathbf{p}\mathbf{v}f(x, p),\end{aligned} \tag{2.23}$$

where $\mathbf{v} = \frac{\mathbf{p}}{p^0}$ is the velocity of the particle. So far, we have been talking about the density and flow of particles, but it is important to realise that in relativistic kinetic theory, these variables can be meaningless, as particles and antiparticles can be continuously produced and destroyed. So instead of particles, we are going to talk about conserved quantum numbers like baryon number, electric charge, strangeness, etc. Then we can talk about the density of baryon number, which is given by the density of baryons and subtracting the density of antibaryons. In this way we can introduce baryon flow. The same argument applies to other conserved quantum numbers. In general, we can introduce a four-stream N^μ for any conserved quantum number [13].

Now we return to our energy density and momentum tensor. With the kinetic theory defined above, the components of the tensor $T^{\mu\nu}$ can be broken down as follows. The 00 component of the energy-momentum tensor is the macroscopic energy density, thus integrating the energy at a given location x

$$T^{00}(x) = \int \mathrm{d}^3\mathbf{p} p^0 f(x,p) = \int \frac{\mathrm{d}^3 p}{E} p^0 p^0 f(x,p). \tag{2.24}$$

The flow of energy is given by

$$T^{0i}(x) = \int \mathrm{d}^3\mathbf{p} p^0 v^i f(x,p) = \int \frac{\mathrm{d}^3 p}{E} p^0 p^i f(x,p). \tag{2.25}$$

The momentum density T^{i0} is given by the total integrated momentum over all the particles

$$T^{i0}(x) = \int \mathrm{d}^3\mathbf{p} p^i f(x,p) = \int \frac{\mathrm{d}^3 p}{E} p^i p^0 f(x,p), \tag{2.26}$$

and the momentum flow is given by

$$T^{ij}(x) = \int \frac{\mathrm{d}^3}{E} \mathbf{p} p^i v^j f(x,p). \tag{2.27}$$

These four relations can be combined into one Lorentz covariant form for the energy momentum tensor

$$T^{\mu\nu}(x) = \int \frac{\mathrm{d}^3\mathbf{p}}{E} p^\mu p^\nu f(x,p), \tag{2.28}$$

The energy momentum tensor has been defined here with contributions from the mass and kinetic energy of the particles.

2.5 Minkowski space and hyperbolic coordinates

To simplify hydrodynamic calculations, we use the Minkowski spacetime. Minkowski spacetime is a 4-dimensional linear vector space with a defined pseudoscalar product in which the coordinates are given $x^\mu = (t, x, y, z)$ and with a metric tensor

$$g^{\mu\nu} = diag(1, -1, -1, -1). \tag{2.29}$$

Hyperbolic coordinates τ, η_s are defined as

$$\tau = \sqrt{t^2 - z^2}, \quad \eta = \operatorname{arctanh}\left(\frac{z}{t}\right), \tag{2.30}$$

and the inverse transformation is a given by

$$t = \tau \cosh \eta, \quad z = \tau \sinh \eta. \tag{2.31}$$

Hyperbolic coordinates are therefore $\tilde{x}^\mu = (\tau, x, y, \eta)$ and the transformation matrix can be calculated according to $R^\alpha_{\ \mu} \equiv \frac{\partial x^\alpha}{\partial \tilde{x}^\mu}$

$$R^\alpha_{\ \mu} = \begin{pmatrix} \cosh\eta & 0 & 0 & \tau\sinh\eta \\ 0 & 1 & 0 & 0 \\ 0 & 0 & 1 & 0 \\ \sinh\eta & 0 & 0 & \tau\cosh\eta \end{pmatrix}, \tag{2.32}$$

then Hyperbolic metric is

$$\tilde{g}_{\mu\nu} = \operatorname{diag}(1, -1, -1, -\tau^2). \tag{2.33}$$

For this special metric we have non-zero Christoffel symbols according to (2.18)

$$\Gamma^\eta_{\tau\eta} = \Gamma^\eta_{\eta\tau} = \frac{1}{\tau}, \ \ \Gamma^\tau_{\eta\eta} = \tau. \tag{2.34}$$

2.6 Relativistic Euler equations

An ideal fluid is defined as a fluid in which all shear stresses are zero. Our goal is to construct a usable decomposition of the momentum energy tensor, where by adding higher-order tensors, we get more accurate results

$$T^{\mu\nu} = T^{\mu\nu}_{(0)} + T^{\mu\nu}_{(1)} + T^{\mu\nu}_{(2)} + ... \tag{2.35}$$

First we consider a fluid that is in local equilibrium and is not affected by external forces. Tensor $T^{\mu\nu}_{(0)}$ corresponds to the ideal fluid. The explicit shape of the tensor $T^{\mu\nu}_{(0)}$ is derived as follows. The energy and momentum tensor must be an effective function of the hydrodynamic degrees of freedom, energy density and pressure - ϵ, p and the four-velocities defined via relation

$$u^\mu = \frac{dx^\mu}{d\tau}, \tag{2.36}$$

where τ proper time, which is given by (2.6) $\mathrm{d}\tau = \mathrm{d}s$. To see what a four-volocity looks like, consider the case of Minkowski spacetime, in which the metric tensor in (pseudo)cartesian coordinates is given by $g_{\mu\nu} = \operatorname{diag}(1, -1, -1, -1)$. In this case the interval $\mathrm{d}s$ to move a point with the speed $\mathbf{v}$ is given

$$(ds)^2 = (dt)^2 - (d\mathbf{x})^2 = (dt)^2 \left(1 - \left(\frac{d\mathbf{x}}{dt}\right)^2\right) = (dt)^2 \left(1 - \mathbf{v}^2\right), \tag{2.37}$$

and thus

$$u^\mu = \frac{\mathrm{d}x^\mu}{\mathrm{d}t}\frac{\mathrm{d}t}{\mathrm{d}s} = \frac{1}{\sqrt{1-\mathbf{v}^2}}\begin{pmatrix}1\\ \mathbf{v}\end{pmatrix} = \gamma(\mathbf{v})\begin{pmatrix}1\\ \mathbf{v}\end{pmatrix}, \tag{2.38}$$

where $\gamma(\mathbf{v})$ is the Lorentz factor. For the non-relativistic case (for small speeds) we get $\gamma(\mathbf{v}) = \frac{1}{\sqrt{1-\mathbf{v}^2}} \approx 1 + \frac{v^2}{2} + \mathcal{O}(\mathbf{v}^4)$ and thus $u^\mu = \begin{pmatrix}1\\ \mathbf{v}\end{pmatrix} + \mathcal{O}(\mathbf{v}^2)$. In the lowest order we consider the energy and momentum tensor in the most general form

$$T_0^{\mu\nu} = f_1(c_1 u^\mu u^\nu + c_2 g^{\mu\nu}) + f_2(c_3 u^\mu u^\nu + c_4 g^{\mu\nu}), \tag{2.39}$$

where c_1, c_2, c_3, c_4 are constants, $f_1 = f_1(x^\mu)$ and $f_2 = f_2(x^\mu)$ scalar function, $u^\mu(x^\mu)$ four-velocity and $g^{\mu\nu}$ metric tensor [43]. In a local rest frame (LRF) near the equilibrium position, the energy and momentum tensor is

$$\langle T^{\mu\nu}\rangle_{(0)LRF} = diag(\epsilon, p, p, p), \tag{2.40}$$

where p is the pressure and ϵ the energy density. This is the only possible combination of vectors and tensors that we have at our derivation. In a local rest frame, the four-velocity vector is $u^\mu = \begin{pmatrix}1\\ \mathbf{0}\end{pmatrix}$ and using the Minkowski metric $g_{\mu\nu} = diag(1, -1, -1, -1)$ we get (2.39)

$$\langle T^{\mu\nu}\rangle_{(0)LRF} = diag(f_1(c_1+c_2)+f_2(c_3+c_4), -f_1c_2-f_2c_4, -f_1c_2-f_2c_4, -f_1c_2-f_2c_4). \tag{2.41}$$

By comparing (2.40) and (2.41) we get

$$\begin{aligned}\left\langle T^{00}\right\rangle_{(0)LRF} &= \epsilon = f_1(c_1+c_2) + f_2(c_3+c_4),\\ \left\langle T^{ii}\right\rangle_{(0)LRF} &= p = -f_1c_2 - f_2c_4, \text{ for } i,j = 1,2,3\end{aligned} \tag{2.42}$$

The solution is chosen so that the function f_1 can be identified with energy density, and the function f_2 with pressure. These equations have solution

$$c_1 = 1,\ c_2 = 0, c_3 = 1, c_4 = -1. \tag{2.43}$$

By inserting (2.43) into (2.42) we get an explicit form of energy and momentum tensor

$$T^{\mu\nu} = (\epsilon + p)u^\mu u^\nu - p g^{\mu\nu}. \tag{2.44}$$

Introducing a *space-like projector*, denoted by $\Delta^{\mu\nu}$, can be helpful in the calculation of equations of motion. We define the projectors as follows

$$\Delta^{\mu\nu} = u^\mu u^\nu - g^{\mu\nu}. \tag{2.45}$$

For any metric tensor $g^{\mu\nu}$, the projectors $\Delta^{\mu\nu}$ are perpendicular to a four-velocity that is always time-like, i.e. $\Delta^{\mu\nu}u_\mu = u^\mu u^\mu u_\mu - g^{\mu\nu}u_\mu = u^\mu - u^\mu = 0$. $\Delta^{\mu\nu}u_\nu = 0$, and further the relation

$$\Delta_{\mu\nu}\Delta^\nu_\rho = (u_\mu u_\nu - g_{\mu\nu})(u^\nu u_\rho - g^\nu_\rho) = g_{\mu\nu}g^\nu_\rho - g_{\mu\nu}u^\nu u_\rho - g^\nu_\rho u_\mu u_\nu + u_\mu u_\rho = \Delta_{\mu\rho}. \tag{2.46}$$

The easiest way to show $\Delta^{\mu\nu}$ is in Minkowski coordinates. If we consider the LRF, the four-velocity has only the first component non-zero, i.e. $u^\mu_{LRF} = (1, \mathbf{0})$, projectors

$\Delta^{\mu\nu} = \mathrm{diag}(0,1,1,1)$ and $u^{\mu}_{LRF}u^{\nu}_{LRF} = \mathrm{diag}(1,0,0,0)$. The second relationship defines the projector in the direction of four-velocity [43]. Using the projectors defined as (2.44), we describe the energy and momentum tensor (2.45) as

$$T^{\mu\nu}_{(0)} = \epsilon u^{\mu}u^{\nu} + p\Delta^{\mu\nu}. \tag{2.47}$$

Then the law of conservation of energy and momentum in LRF are

$$\nabla_{\mu}T^{\mu\nu}_{(0)} = 0. \tag{2.48}$$

Let us look separately at the time-like and space-like part (2.48), by projecting u^{ν} and $\Delta^{\nu\alpha}$ onto (2.48)

$$u_{\nu}\nabla_{\mu}T^{\mu\nu}_{(0)} = 0, \tag{2.49}$$

$$\Delta^{\alpha}_{\nu}\nabla_{\mu}T^{\mu\nu}_{(0)} = 0. \tag{2.50}$$

For the first equation we get

$$\begin{aligned} u_{\nu}\nabla_{\mu}T^{\mu\nu}_{(0)} &= u_{\nu}\nabla_{\mu}(\epsilon u^{\mu}u^{\nu} + p\Delta^{\mu\nu}) = u_{\nu}\nabla_{\mu}(\epsilon u^{\mu}u^{\nu}) + u_{\nu}\nabla_{\mu}(p\Delta^{\mu\nu}) = \\ &= u_{\nu}u^{\nu}u^{\mu}\nabla_{\mu}\epsilon + \epsilon u_{\nu}u^{\mu}\nabla_{\mu}u^{\nu} + \epsilon u_{\nu}u^{\nu}\nabla_{\mu}u^{\mu} + pu_{\nu}\nabla_{\mu}\Delta^{\mu\nu} + u_{\nu}\Delta^{\mu\nu}\nabla_{\mu}p = \\ &= u^{\mu}\nabla_{\mu}\epsilon + \epsilon\nabla_{\mu}u^{\mu} + p\nabla_{\mu}u^{\mu} \\ &= (p+\epsilon)\nabla_{\mu}u^{\mu} + u^{\mu}\nabla_{\mu}\epsilon = 0, \end{aligned} \tag{2.51}$$

where $u_{\nu}\nabla_{\mu}u^{\nu} = \frac{1}{2}\nabla_{\mu}(u_{\nu}u^{\nu}) = \frac{1}{2}\nabla_{\mu}1 = 0$. For the second equation, we obtain

$$\begin{aligned} \Delta^{\alpha}_{\nu}\nabla_{\mu}T^{\mu\nu}_{(0)} &= \Delta^{\alpha}_{\nu}\nabla_{\mu}(\epsilon u^{\mu}u^{\nu} + p\Delta^{\mu\nu}) = \Delta^{\alpha}_{\nu}\nabla_{\mu}(\epsilon u^{\mu}u^{\nu}) + \Delta^{\alpha}_{\nu}\nabla_{\mu}(p\Delta^{\mu\nu}) = \\ &= \Delta^{\alpha}_{\nu}u^{\mu}u^{\nu}\nabla_{\mu}\epsilon + \epsilon\Delta^{\alpha}_{\nu}u^{\mu}\nabla_{\mu}u^{\nu} + \epsilon\Delta^{\alpha}_{\nu}u^{\nu}\nabla_{\mu}u^{\mu} + p\Delta^{\alpha}_{\nu}\nabla_{\mu}\Delta^{\mu\nu} + \Delta^{\alpha}_{\nu}\Delta^{\mu\nu}\nabla_{\mu}p = \\ &= \epsilon u^{\mu}\nabla_{\mu}u^{\alpha} + pu^{\mu}\nabla_{\mu}u^{\alpha} - \Delta^{\mu\alpha}\nabla_{\mu}p = \\ &= (\epsilon+p)u^{\mu}\nabla_{\mu}u^{\alpha} - \Delta^{\mu\alpha}\nabla_{\mu}p = 0, \end{aligned} \tag{2.52}$$

where $\Delta^{\alpha}_{\nu}\nabla_{\mu}u^{\nu} = (u^{\alpha}u_{\nu} - g^{\alpha}_{\nu})\nabla_{\mu}u^{\nu} = -g^{\alpha}_{\nu}\nabla_{\mu}u^{\nu} = -\nabla_{\mu}(g^{\alpha}_{\nu}u^{\nu}) = -\nabla_{\mu}u^{\alpha}$. In the next step it is useful to introduce *derivative projection*

$$D \equiv u^{\mu}\nabla_{\mu}, \tag{2.53}$$

$$\nabla^{\alpha}_{\perp} \equiv \Delta^{\mu\alpha}\nabla_{\mu}, \tag{2.54}$$

where $\nabla_{\mu} = u_{\mu}D + \nabla^{\alpha}_{\perp}$ and $\nabla_{\mu}u^{\mu} = (u_{\mu}D + \nabla^{\alpha}_{\perp})u^{\mu} = \nabla^{\alpha}_{\perp}u^{\mu}$. Using (2.53) and (2.54) we convert (2.51) and (2.52) to the final form.

$$D\epsilon + (\epsilon+p)\nabla^{\perp}_{\mu}u^{\mu} = 0, \tag{2.55}$$

$$(\epsilon+p)Du^{\alpha} + \nabla^{\alpha}_{\perp}p = 0. \tag{2.56}$$

Using the equation of state $p = p(\epsilon)$, it is possible to use $\nabla^{\alpha}_{\perp}p = \frac{\partial p(\epsilon)}{\partial\epsilon}\nabla^{\alpha}_{\perp}\epsilon$, to rewrite (2.55) and (2.56) into the form

$$\begin{aligned} D\epsilon + (\epsilon+p)\nabla^{\perp}_{\mu}u^{\mu} &= 0, \\ (\epsilon+p)Du^{\alpha} - c_s^2\nabla^{\alpha}_{\perp}\epsilon &= 0, \end{aligned} \tag{2.57}$$

where c_s can be recognized as the speed of sound in a fluid

$$c_s^2(\epsilon) = \frac{\partial p(\epsilon)}{\partial\epsilon}. \tag{2.58}$$

2.6.1 Application: Transition to non-relativistic Euler equation

Our goal is to develop a relativistic hydrodynamics framework that aligns with classical hydrodynamics. When we take the non-relativistic limit, where $|\mathbf{v}| \ll 1$, we recover the classical Euler equation and continuity equation. In the case of a velocity vector u^μ, the components are approximately $u^0 \sim 1$ and $u^i \sim v^i$.

$$\begin{aligned} D = u^\mu \nabla_\mu = u^0 \partial_0 + u^i \partial_i \xrightarrow{|\mathbf{v}| \to 0} \partial_t + v^i \partial_i + \mathcal{O}(|\mathbf{v}^2|), \\ \nabla^i_\perp = \Delta^{i\mu} \nabla_\mu \xrightarrow{|\mathbf{v}| \to 0} \partial_i + \mathcal{O}(|\mathbf{v}^2|). \end{aligned} \tag{2.59}$$

Since we consider the non-relativistic limit, the energy density of ϵ is much greater than the pressure of $\epsilon \gg p$ and the energy density corresponds to $\epsilon \sim \rho$. Then, using (2.59), we rewrite Euler's relativistic equations (2.56) into nonrelativistic ones like

$$(\partial_t + v^i \partial_i)\rho + \rho \partial_i v^i = \partial_t \rho + \nabla(\rho \mathbf{v}) = 0, \tag{2.60}$$

$$\rho(\partial_t v^i + v^i \partial_i v^i) + \partial_i p = \partial_t \mathbf{v} - \mathbf{v} \cdot \nabla \mathbf{v} = -\frac{1}{\rho} \nabla p. \tag{2.61}$$

The equation (2.60) corresponds to the equation of continuity and the equation (2.61) corresponds to the classical equation of motion for the ideal fluid (Euler's equation for the movement of the ideal fluid). [43]

2.6.2 Bjorken model

Now, let us consider the hydrodynamic description of the quark-gluon plasma (QGP) generated by ultrarelativistic nuclear collisions at the RHIC or LHC accelerator. We only consider very energetic nuclei that move at a high speed. At $t = 0$ and $z = 0$, these nuclei collide. The simplest model for describing hydrodynamic expansion is based on Bjorken's scenario [18], in which a distance of z at time t, matter moves at $v_z = \frac{z}{t}$. The movement of the nuclei is along the z axis. The transverse expansion and dynamics in this plane are neglected $v_x = v_y = 0$. The next step is to introduce hyperbolic coordinates (2.30). Phase variables will be ϵ and p will only be functions of τ z(2.30) because in the z axis the continuum has a constant speed of $v_z \sim v_z^0$. The four-vector velocity u^μ written in hyperbolic coordinates

$$u^\mu = (u^\tau, u^x, u^y, u^\eta) = (\partial_\tau \tau, \partial_\tau x, \partial_\tau y, \partial_\tau \eta) = (1, 0, 0, 0)\,. \tag{2.62}$$

For hyperbolic coordinates we have given the metric tensor (2.33) and the only non-zero Christoffel symbols are (2.34). In the next step we will look at the covariant derivative after the components of the energy and momentum tensor. Together with

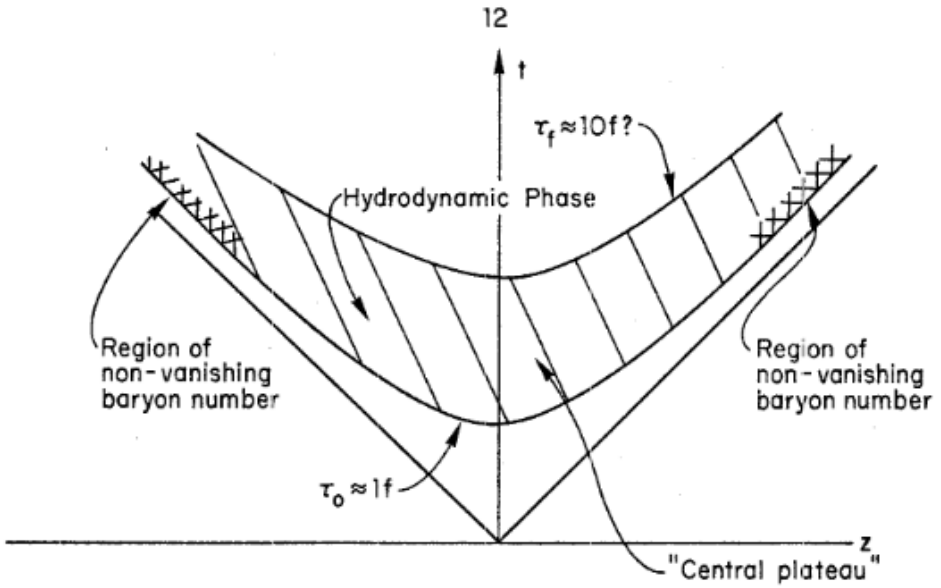

Figure 2.1: A spatial diagram of QGP development in central rapidity. Taken from [18].

non-zero Christofel symbols (2.34) we get

$$\begin{aligned}
\nabla_\mu T^{\mu\tau} &= \partial_\mu T^{\mu\tau} + \Gamma^\mu_{\lambda\mu} T^{\lambda\tau} + \Gamma^\tau_{\lambda\mu} T^{\mu\lambda} = 0, \\
&= \partial_\mu T^{\mu\tau} + \frac{1}{\tau} T^{\tau\tau} + \tau T^{\eta} = 0, \\
\nabla_\mu T^{\mu x} &= \partial_\mu T^{\mu x} + \Gamma^\mu_{\lambda\mu} T^{\lambda x} + \Gamma^x_{\lambda\mu} T^{\mu\lambda} = 0, \\
&= \partial_\mu T^{\mu x} + \frac{1}{\tau} T^{\tau x} = 0, \\
\nabla_\mu T^{\mu y} &= \partial_\mu T^{\mu y} + \Gamma^\mu_{\lambda\mu} T^{\lambda y} + \Gamma^y_{\lambda\mu} T^{\mu\lambda} = 0, \\
&= \partial_\mu T^{\mu y} + \frac{1}{\tau} T^{\tau y} = 0, \\
\nabla_\mu T^{\mu\eta} &= \partial_\mu T^{\mu\eta} + \Gamma^\mu_{\lambda\mu} T^{\lambda\eta} + \Gamma^\eta_{\lambda\mu} T^{\mu\lambda} = 0, \\
&= \partial_\mu T^{\mu\eta} + \frac{3}{\tau} T^{\tau\eta} = 0.
\end{aligned} \tag{2.63}$$

These equations can be solved numerically in principle. If we limit ourselves to a one-dimensional Bjorken flow, where the four-velocity is gived by (2.62) and the individual non-zero components of the momentum tensor and energy are given as

$$T^{\tau\tau} = \epsilon,\ T^{xx} = p,\ T^{yy} = p,\ T^{\eta\eta} = \frac{p}{\tau^2}, \tag{2.64}$$

where we used (2.5). Equations (2.63) have a simpler form and we get

$$\begin{aligned}
\partial_\mu T^{\mu\tau} + \frac{1}{\tau} T^{\tau\tau} + \tau T^{\eta\eta} &= \partial_\tau T^{\tau\tau} + \frac{1}{\tau}\epsilon + \tau \frac{1}{\tau^2} p, \\
&= \frac{\partial \epsilon}{\partial \tau} + \frac{\epsilon + p}{\tau} = 0.
\end{aligned} \tag{2.65}$$

If we consider the constant speed of sound in the form $p = c_s^2\epsilon$ and the equation of state as a function of $p = p(\epsilon)$, we get an analytical solution to the differential equation

$$\frac{\partial\epsilon}{\partial\tau} + \frac{(1+c_s^2)\epsilon}{\tau} = 0 \Rightarrow \epsilon(\tau) = \epsilon(\tau_0)\left(\frac{\tau_0}{\tau}\right)^{(1+c_s^2)}, \tag{2.66}$$

where $\tau_0 = 1$ fm/c is the initial condition. We see that the density of energy decreases from its initial value with an exponent that depends on the speed of sound. For the ideal relativistic gas $c_s^2 = \frac{1}{3}$, we have

$$\epsilon \sim \tau^{-\frac{4}{3}}. \tag{2.67}$$

It is obvious that further refinement and approximation to the real world can be achieved by including transverse expansion effects.

2.7 Relativistic Navier-Stokes equations

Now we will create further development of the energy and momentum tensor. If we do not neglect the viscosity effect, we have to consider the more general shape of the tensor $T^{\mu\nu}$. Consider a tensor shaped like

$$T^{\mu\nu} = T^{\mu\nu}_{(0)} + T^{\mu\nu}_{(1)}, \tag{2.68}$$

where $T^{\mu\nu}_{(0)}$ is the contribution of the energy and momentum tensor of the ideal fluid, and $T^{\mu\nu}_{(1)}$ includes the viscous part that causes dissipation in the system. This tensor can be constructed from gradients the $\nabla^\perp_\mu$ of state variables ϵ and u^μ in the form:

$$\nabla^\perp_\mu u^\mu,\ \nabla^\perp_\mu \ln\epsilon,\ \nabla^\perp_\mu u_\nu, \tag{2.69}$$

where the building blocks (2.69) are combined from the zero order ϵ, u^μ and $g^{\mu\nu}$. Now it is important to discuss the meaning of the four-velocity u^μ. In relativistic mechanics, the flow of energy necessarily involves the flow of matter. But on the other hand, if there is a heat flow, then the definition of velocity using the density of the mass flow is not necessary correct. The definition for the Landau speed condition that we will use in this case will be - in the local rest frame (LRF) the momentum of the element is zero and the energy, expressed using other thermodynamic variables, is expressed in the same way as when dissipative processes are not present. In other words, in the LRF component $T^{00}_{(1)} = T^{0i}_{(1)} = 0$. In the LRF it is true that $u^i = 0$, in any system we get

$$u_\mu T^{\mu\nu}_{(1)} = 0. \tag{2.70}$$

So we can see from (2.68) and (2.70) that the expected value of the energy tensor meets *Landou's definition of velocity*

$$u_\mu T^{\mu\nu} = \epsilon u^\nu. \tag{2.71}$$

Since $T^{\mu\nu}_{(1)}$ is a symmetric tensor of the second order, the only possible combinations of building blocks are $\Delta_{\mu\nu}\nabla^\perp_\lambda u^\lambda$ and the symmetric combination

$$\nabla^\perp_{(\mu} u_{\nu)} = \frac{1}{2}(\nabla^\perp_\mu u_\nu + \nabla^\perp_\nu u_\mu). \tag{2.72}$$

For later purposes, it is appropriate to consider two linear combinations of these two members, namely

$$\begin{aligned} &\Delta^{\mu\nu}\nabla_\lambda^\perp u^\lambda, \\ &\sigma^{\mu\nu} = 2\nabla_\perp^{(\mu} u^{\nu)} - \frac{2}{3}\Delta^{\mu\nu}\nabla_\lambda^\perp u^\lambda, \end{aligned} \tag{2.73}$$

where tensor $\sigma^{\mu\nu}$ has zero trace, $g_{\mu\nu}\sigma^{\mu\nu} = 0$. Now we can break down the first-order contribution of the energy and momentum tensor development $T^{\mu\nu}_{(1)}$ as

$$T^{\mu\nu}_{(1)} = -\eta\sigma^{\mu\nu} - \zeta\Delta_{\mu\nu}\nabla_\lambda^\perp u^\lambda, \tag{2.74}$$

where $\eta(\epsilon)$ and $\zeta(\epsilon)$ are hydrodynamic coefficients dependent on the density of ϵ, which can be recognized as the coefficient of shear and bulk viscosity. We get the equations of motion in a similar way as for relativistic Euler equations

$$\nabla_\mu T^{\mu\nu} = \nabla_\mu(T^{\mu\nu}_{(0)} + T^{\mu\nu}_{(1)}) = 0, \tag{2.75}$$

this equation can be rewritten $\nabla_\mu(T^{\mu\nu}_{(0)} = -\nabla_\mu T^{\mu\nu}_{(1)})$. Using projectors we get

$$\begin{aligned} &D\epsilon + (\epsilon + P)\left(\nabla_\lambda^\perp u^\lambda\right) = \frac{\eta}{2}\sigma^{\mu\nu}\sigma_{\mu\nu} + \zeta\left(\nabla_\lambda^\perp u^\lambda\right)^2, \\ &(\epsilon + P)Du^\alpha + c_s^2\nabla_\perp^\alpha\epsilon = \Delta_\nu^\alpha\nabla_\mu\left(\eta\sigma^{\mu\nu} + \zeta\delta^{\mu\nu}\left(\nabla_\lambda^\perp u^\lambda\right)\right). \end{aligned} \tag{2.76}$$

These equations are known as the relativistic equations of a viscous fluid or the Navier-Stokes equations. Unlike their non-relativistic versions, they are useful only for a small class of problems that can be solved analytically. Their practical numerical use is limited by the fact that they violate causality.

2.8 Israel-Stewart formalism

The Israel-Stewart formalism [28, 43, 47] is a theoretical framework for describing the behaviour of relativistic fluids, such as those found in high-energy nuclear collisions or astrophysical systems. The dynamics of the fluid are described by a set of equations that take into account the dissipative effects of the fluid. These dissipative effects include shear viscosity, which causes the fluid to resist deformation, and bulk viscosity, which causes the fluid to resist compression.

We are able to add more higher terms to the expansion (2.68) and get further and further away from the static equilibrium. It is convenient to introduce a notation where we divide the corrections to the zero series of energy and momentum tensor $T^{\mu\nu}_{(0)}$ into a part with a zero trace $\pi^{\mu\nu}$ and a non-zero trace $\Delta^{\mu\nu}\Pi$. The energy and momentum tensor in any order is

$$\begin{aligned} &\langle T^{\mu\nu}\rangle = T^{\mu\nu}_{(0)} + \pi^{\mu\nu} + \Delta^{\mu\nu}\Pi, \\ &\pi^{\mu\nu} = T^{<\mu\nu>}_{(1)} + T^{<\mu\nu>}_{(2)} + ..., \quad \Pi = \frac{1}{3}(T^\mu_{(1)\mu} + T^\mu_{(2)\mu}) + ..., \end{aligned} \tag{2.77}$$

where $\pi^{\mu\nu}$ is called a shear tensor and Π is called a bulk tensor. The upper designation of the indexes $A^{<\mu\nu>}$ is understood as

$$A^{<\mu\nu>} \equiv \frac{1}{2}\Delta^{\mu\lambda}\Delta^{\nu\rho}(A_{\lambda\rho} + A_{\rho\lambda}) - \frac{1}{3}\Delta^{\mu\nu}\Delta^{\lambda\rho}A_{\lambda\rho}, \tag{2.78}$$

If we go back to (2.74), it implies

$$\pi^{\mu\nu} = -\eta\sigma^{\mu\nu}, \tag{2.79}$$

$$\Pi = -\zeta\nabla^{\perp}_{\lambda}u^{\lambda}, \tag{2.80}$$

which are sometimes referred to as constitutive (first order) equations. Diagonal components of the spatial part of tensor $T^{\mu\nu}$, which for ideal fluids had an interpretation of local pressure P, have imbalanced corrections. So we have to include corrections of the effective pressure tensor $P\delta^i_j + \pi^i_{j,LRF} + \delta^i_j\Pi$ such that the effective pressure in the i direction is [43]

$$P^{(i)}_{eff} = P + \pi^i_{i,LRF} + \Pi, \tag{2.81}$$

where $\pi^{\mu\nu}_{LRF}$ is a shear tensor transformed into a LRF.

The spectral analysis of relativistic Navier Stokes equations shows acausality, which causes instabilities in numerical calculation. Current and well-know viscous hydro codes use following structure of hydrodynamic viscous equation

$$D\pi^{\mu\nu} = -\frac{\pi^{\mu\nu} - \pi^{\mu\nu}_{NS}}{\tau_\pi} - \frac{4}{3}\pi^{\mu\nu}\partial_\alpha u^\alpha, \tag{2.82}$$

$$D\Pi = -\frac{\Pi - \Pi_{NS}}{\tau_\Pi} - \frac{4}{3}\Pi\partial_\alpha u^\alpha, \tag{2.83}$$

$$\tag{2.84}$$

where the parameters τ_π respectively τ_Π are relaxation times respectively linear functions of the corresponding viscosity, that fulfil

$$\pi^{\mu\nu} = 2\eta\nabla_{\langle\mu}u_{\nu\rangle} \implies \tau_\pi D\pi^{\mu\nu} + \pi^{\mu\nu} = \pi^{NS}, \tag{2.85}$$

$$\Pi = -\zeta\nabla_\alpha u^\alpha \implies \tau_\Pi D\Pi + \Pi = \Pi^{NS}. \tag{2.86}$$

While in Navier Stokes hydrodynamics the viscous terms are bound to the velocity gradients by fixed relationships (2.79) and (2.80), after generalisation they are independently dynamic quantities and we have added other equations (2.82) and (2.83) for them. These equations are know as Israel-Stewart equations. We will to use them in the vHLLE [29, 30] model that is used in this work.

Chapter 3

Hydrodynamic modelling

The hydrodynamic modelling of heavy ion collisions is usually provided in 3 or 4 steps. The evolution of the hot dense matter from the time of the collision to the time of kinetic freeze-out is currently often described by the so-called hybrid models.

The main advantage of these models is that each stage of the medium expansion is described by a different model which is most accurate for a given stage. Firstly, the initial condition [1] (commonlu known as IC) are created (an energy density profile, an entropy profile,..), then the initial state is transformed into a viscous fluid, which is developed by a hydrodynamic code until the production of particles and their rescattering. In this work, we run simulations with the hydrodynamic code called vHLLE, which does not contain the initial condition model and the final transport model. Thus these models must be included. Let us firstly mention some general facts about the hybrid model. Then we will describe each of the models.

3.1 Hybrid model

Hybrid models are commonly used to explain the development of hot and dense matter from the moment of collision until kinetic freeze-out. These models have a significant advantage in that each phase of the medium's expansion is described by the most accurate model. The dilute later stage following particle hadronization is described by a hadronic transport model like SMASH [53] and UrQMD [19]. The stages of the hybrid model are illustrated in Fig. 3.1. By comparing the hybrid model with measured data, it was discovered that analyzing the results of simulation event by event and then examining the ensemble, as with actual data,leads to more appropriate comparisons and predictions.

The hybrid model, however, faces a significant challenge in connecting two distinct approaches that have different degrees of freedom. In the current approach, the hybrid models solve fluid dynamics regardless of the boundary condition provided by cascade models, which assumes a vacuum at infinity. The point at which the fluid dynamic model switches to the transport model is determined a posteriori, once the

[1] It depends on which model is used.

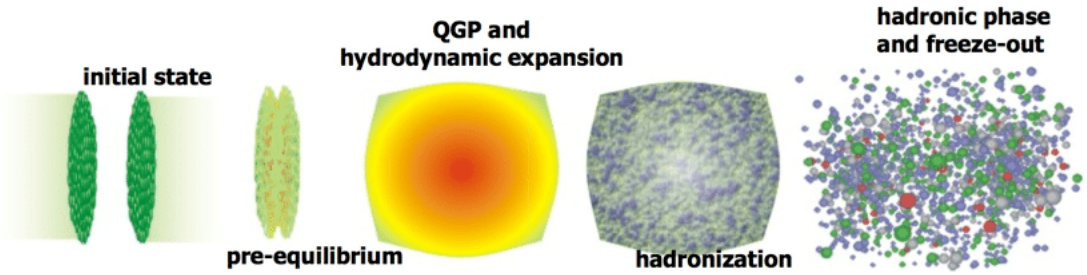

Figure 3.1: Schematictime evolution of a heavy ion collision. Taken from [51].

fluid evolution is complete. This switching surface typically satisfies conditions of constant temperature T, energy density ϵ, or time t. The distributions of particles on the switching hypersurface Σ^μ are calculated using the Cooper-Frye formula as follows formula [24]

$$E\frac{\mathrm{d}^3N_i}{\mathrm{d}^3p} = \int \mathrm{d}\Sigma^\mu p^\mu f(p\cdot u(x), T(x), \mu_i(x))., \tag{3.1}$$

where E is energy, T is temperature, μ_i is chemical potential and f is a distribution function.

It is important to note that in the hybrid model, the creation of particles from fluid, also known as particlization, should not be mistaken for freeze-out. This is because, as previously stated, there are no inelastic or elastic collisions after thermal freeze-out, only decays of resonances. Therefore, the transport stage that includes resonance decays must be incorporated. Additionally, in the real collision there is no clear point of hadronization due to the crossover phenomenon. As a result, in a simulation the switching surface is often selected when hadronization is complete.

3.1.1 Initial state model

The initial state models simulate or parametrize the initial collision of the colliding nuclei. The collision takes place according to the physical approach of given model. The output of the initial state generator is usually an energy density profile or entropy profile. There are plenty of the initial state models such as SMASH [53], UrQMD [19], Glissando [22], Trento [37], Trento3d [31, 32] and more. The transport models like UrQMD or SMASH aim at the complete description of the whole collision process, but can also be used to simulate just the collisions of the incident nucleons from which then initial conditions for fluid dynamics are determined. The Trento appears to be the best choice of initial state models for the description of LHC energies.

Trento

Trento (Reduced Thickness Event-by-event Nuclear Topology) [32, 37] a simple, fast model for the initial conditions of high-energy nuclear collisions of proton-proton,

proton-Nucleon and Nucleon-Nucleon (pp, pA and AA). It is a parametric initial condition model, that is based on eikonal entropy deposition via a reduced thickness function. Trento is an effective model, intended to generate realistic Monte Carlo initial entropy profiles without assuming specific physical mechanisms for entropy production, pre-equilibrium dynamics, or thermalization. Trento introduces a generalised ansatz for the entropy density deposition from the participant nucleons as follows

$$T_R(p; T_A, T_B) \equiv \left(\frac{T_A^p + T_B^p}{2} \right)^{1/p}, \tag{3.2}$$

where T_A, T_B are the thickness profiles of the two incoming nuclei and p is a dimensionless parameter which interpolates between the simplified functional forms of the initial entropy density profile in different initial state models. For instance, $p = 1$ corresponds to a Monte Carlo wounded nucleon model. The default is $p = 0$, which corresponds to the geometric mean. Trento model is very suitable for many studies of pA and AA collision at the top RHIC and LHC energies.

Generating of the initial conditions is provided by specifying both types of projectiles. The types of incoming projectile are for example proton p, deuteron d, two types of copper Cu, two variants of xenon 129 Xe, two types of gold 197 Au, lead 208 Pb, and three types of uranium U. In this work, we focus on the simulation of Pb-Pb collisions. Another mandatory Trento option is the number of events **N**. There will be 400 events in our simulation. This work is focused on event-by-event observables that are influenced by initial state fluctuations. Another mandatory Trento inputs must be sat. The first of them is the cross-section σ_{NN}. In physics, the cross section is a measure of the probability that a specific process will take place when some kind of radiant excitation (e.g. a particle beam, sound wave, light, or an X-ray) intersects a localized phenomenon (e.g. a particle or density fluctuation). Furthermore, the range of impact parameters b has to be set (minimum impact parameter b_{min} and maximum impact parameter b_{max}). The reduced thickness parameter **p**, which is discussed above, has to be set.

Trento has optional parameters as well. As optional parameter the Gaussian nucleon width **w** can be used. It is defined as follows

$$T_{nucleon}(x, y) = \frac{1}{2\pi w^2} \exp\left(-\frac{x^2 + y^2}{w^2} \right) \tag{3.3}$$

The minimum nucleon-nucleon distance **d** for Woods-Saxon nuclei (spherical and deformed) is another optional input parameter. When nonzero, if a sampled nucleon lands too close to a previously sampled nucleon, its angular position is resampled until it lands far enough away. The radius is not resampled, since this would effectively modify the Woods-Saxon distribution.

Another parameter is gamma distribution shape parameter **k** for nucleon thickness fluctuations. Fluctuations are implemented by multiplying the density of each nucleon (or nucleon constituent) by a random weight **w**. The weights are sampled from a gamma distribution with the scale parameter fixed so that the mean is one

$$P_k(w) = \frac{k^k}{\Gamma(w)} w^{k-1} e^{-kw} \tag{3.4}$$

The default is $\mathbf{k} = 1$, which corresponds to an exponential distribution. For small $\mathbf{k}$, the distribution has a long tail, leading to large fluctuations. For large $\mathbf{k}$, the distribution becomes a narrow Gaussian, and eventually a delta function for very large values.

Another parameter is a number of constituents inside the nucleon $\mathbf{m}$. The default is $\mathbf{m} = 1$, which means the nucleon is a single Gaussian. Setting the constituent number $\mathbf{m} > 1$ divides the nucleon into Gaussians, each of width $\mathbf{v}$. The constituent positions are sampled from the probability distribution

$$P(x, y) = \frac{1}{2\pi r^2} \exp\left(-\frac{(x-\bar{x})^2 + (y-\bar{y})^2}{2r^2}\right) \tag{3.5}$$

where $(\bar{x}, \bar{y})$ is the transverse position of the parent nucleon, and r is a constituent dispersion width.

Last parameter of optional settings is Gaussian constituent width $\mathbf{v}$, which is defined

$$T_{constit}(x, y) = \frac{1}{2\pi v^2} \exp\left(-\frac{x^2 + y^2}{2v^2}\right) \tag{3.6}$$

By default, the constituent width is set equal to the nucleon width. It can take any positive real value, but it must not be set larger than the nucleon width. More details about the Trento model can be found in [37].

Trento3d

Trento3d [31, 32] is a three-dimensional initial condition model for high-energy nuclear collisions. It is a spatial extension of the original Trento. The Trento model has been very successful describing observables at midrapidity. Trento3d is a three-dimensional initial condition model for high-energy nuclear collisions Boost-invariance may not hold if the initial density of participants is asymmetrical ($T_A(x_\perp) = T_B(x_\perp)$), and dynamic fluctuations can also generate asymmetry. The contributions that are and are not included in the model are the following:

- In collisions where the asymmetry is present, such as non-central A-A and p-A, there is an imbalance in the local thickness functions.
- The model does not include dynamical fluctuations or initial flow in the z-direction.

Thus, in the extended Trento model, asymmetry arises only from the imbalance between T_A and T_B. The decomposition of density entropy $s(x, \eta_s)$ at the hydrodynamic starting time τ_0 can be expressed as follows

$$s(x, \eta_s)|_{\tau=\tau_0} = f(T_A(x), T_B(x)) \times g(T_A(x), T_B(x), \eta_s), \tag{3.7}$$

where the function f is the entropy production at mid-rapidity as explain above [31]. The function g parametrizes the rapidity-dependence and is always normalized

such that $g(\eta_s = 0) = 1$ so that it reduces to the original model at mid-rapidity. The g function is parameterised in terms of rapidity and then transformed to the space-time rapidity [31]

$$g(x, \eta_s) = g(y, T_A(x), T_B(x)) \frac{J \cosh \eta_s}{\sqrt{1 + J^2 \sinh^2 \eta_s}}, \tag{3.8}$$

where the species-dependent factor (Jacobian) J is replaced with an effective value $J \approx \langle p_t \rangle / \langle m_t \rangle$. To relate the asymmetry of $g(y)$ to the difference of T_A, T_B, it is parametrized by the cumulants of g as functions of T_A, T_B. The $g(y)$ function is then reconstruct using its first three cumulants (mean μ, standard deviation σ and skewness γ) by

$$\begin{aligned} g(x, y) &= \mathcal{F}^{-1}\{\tilde{g}(x, k)\}, \\ \log(\tilde{g}) &= i\mu k - \frac{1}{2}\sigma^2 k^2 - \frac{1}{6} i\gamma\sigma^3 k^3 e^{\frac{1}{2}\sigma^2 k^2} + ..., \end{aligned} \tag{3.9}$$

where $\mathcal{F}^{-1}$ is inverse Fourier transformation and for the skewness term, it an exponential factor is included that systematically includes higher order cumulants to regulate the behaviour of the function at large rapidities. The mean, standard deviation, and the skewness are parametrized as follows

- For the mean parameter, it is proportional to the centre of mass rapidity of the local participant density $\mu = \mu\eta_{cm}$
- The standard deviation is a global parameter independent of the transverse location $\sigma = \sigma_0$, but only a function of the center-of-mass energy.
- For the skewness, there is not a preferred form, so there are two parametrizations. These two choices are termed "relative skewness" and "absolute skewness":
  - The "relative skewness" parametrization γ_r:

$$A(T_A, T_B) = \gamma_r \frac{T_A - T_B}{T_A + T_B} \tag{3.10}$$

  - The "absolute skewness" parametrization γ_a:

$$A(T_A, T_B) = \gamma_r \frac{T_A - T_B}{T_0}, \tag{3.11}$$

    where $T_0 = 1$ fm^2, so that γ is a dimensionless parameter. More details about the Trento3d model can be found in [31]. The parameters in our simulations will be chosen according to [31].

3.1.2 Hydrodynamic model

The observation of significant elliptic flow in heavy ion collisions was a signal of the hydrodynamic behaviour of the medium created. Initially, the ideal hydrodynamics approach, which did not consider viscous effects, was employed to describe heavy ion collisions and was found to be effective. However, a more accurate description of the experimental data was obtained using viscous hydrodynamics with a low shear viscosity to entropy density ratio η/s. It should be noted that hydrodynamics can only be applied when the mean free path is short relative to the system size.

vHLLE

Generally, most of the well-know hydrodynamic the space-time into cells according to some lattice. The initial state needs to be converted to an energy density profile of a viscous fluid. The energy momentum tensor is created and divided into a spatial lattice. The fluid is then developed by viscous hydrodynamic equations until a critical level of energy density is reached (until particlisation). Our hydrodynamic model is called vHLLE (viscous Harten-Lax-van Leer-Einfeld), for details see [23, 29, 30], which is relativistic hydrodynamic viscous model. The vHLLE model solves the Israel-Stewart equations of relativistic viscous hydrodynamics in 3 + 1 dimensions, namely by introducing conditions for conservation of energy-momentum and baryon number as a current four-vector

$$\nabla_\mu T^{\mu\nu} = 0, \quad \nabla_\mu N^\mu = 0, \tag{3.12}$$

where ∇_μ donates the covariant derivative. Then the evolution for the shear tensor is given

$$\langle u^\lambda \nabla_\lambda \pi^{\mu\nu} \rangle = -\frac{\pi^{\mu\nu} - \pi^{\mu\nu}_{NS}}{\tau_\pi} - \frac{4}{3}\pi^{\mu\nu}\nabla_\lambda u^\lambda, \tag{3.13}$$

where $\pi^{\mu\nu}_{NS}$ is the Navier-Stokes shear tensor shear stress tensor and $\langle \cdots \rangle$ the brackets denote the traceless and orthogonal to u_μ part of the tensor. In addition to energy and momentum, charge densities are explicitly promoted into the equation of state, so it is suitable for simulating the expansion of matter with finite baryon density. This code retains the ability to solve ideal equations hydrodynamics at the limit of zero viscosity using the Godunov algorithm. The hyperbolic coordinates are used to describe the prevailing expansion in the longitudinal direction.

3.1.3 Particle production model

The last part of heavy ion modelling is sampling and production of particles, which is provided by so-called hadronSampler model. When the fluid becomes more diluted, hydrodynamics is not valid anymore. The system reaches critical energy densidty and the hydrodynamic evolution stops. Production of the particles is based on (3.1). In Figure 3.2, transition between a fluid and a particle gas on hypersurface Σ^μ is depicted. The created particles are influenced by resonance decays and scattering. The model which simulates the post processes after hadronisation is called SMASH.

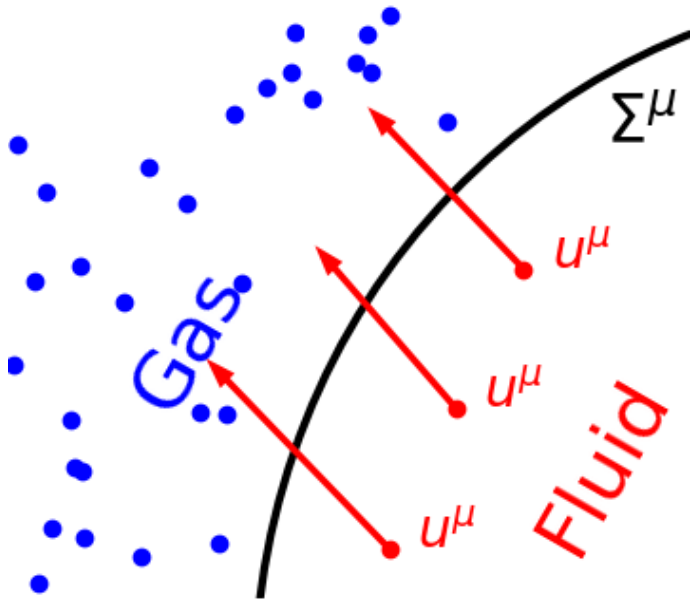

Figure 3.2: Transition from fluid to the particle gas.

SMASH

SMASH (Simulating Many Accelerated Strongly-interacting Hadrons) [53] is a relativistic hadronic transport approach for the dynamical description of heavy ion reactions. It is a model which includes the effects of the hot and dense matter such as manybody interactions. It provides an effective solution of the relativistic Boltzmann equation

$$p^\mu \partial_\mu f_i(x,p) + m_i F^\alpha \partial^p_\alpha f_i(x,p) = C^i_{coll}, \tag{3.14}$$

where C^i_{coll} is the collision term, $f_i(x,p)$ is a one-particle distribution function, F^α is the force experienced by individual particles and m_i is the particle mass. The relativistic Boltzmann equation describes the evolution of the one-particle distribution function of an ideal gas in the phase space spanned by the space-time coordinates $x^\mu = (t, -\vec{x})$ and momentum four-vectors $p^\mu = (p^0, -\vec{p})$ of the particles. One of the major challenges for solving the Boltzmann equation in a relativistic situation is to define an appropriate collision criterion. The criterion of a collision is defined as follows

$$d < d_{int} = \sqrt{\frac{\sigma_{tot}}{\pi}}, \tag{3.15}$$

where σ_{tot} is total cross section of the collision. This is a crucial part for our hybrid package.

SMASH Hadronsampler [30, 44] is used in hybrid models. It provides an interface between the macroscopic hydrodynamic evolution of the fireball and the hadronic afterburner. During the hydrodynamic evolution a hypersurface of constant energy density is created on which the particlisation is placed.

Chapter 4

Results

As the name of the project says, we will focus on Pb+Pb collisions at $\sqrt{s_{NN}} = 2.76$ TeV and $\sqrt{s_{NN}} = 5.02$ TeV. In order to study the behaviour of the elliptic flow, namely the fluctuation in magnitude and its direction, it is necessary to perform the calibration of the hybrid package. Our hybrid package consists of Trento and Trento3d as initial state model, vHLLE as hydrodynamic part and SMASH as afterburner model.

4.1 Simulation with Trento3d

In this section, we will focus on simulation with Trento3d as intial state. As mentioned in Chapter 3, Trento3d is a 3-dimensional extension of original Trento. In Table 4.1, the initial parameters can be found. Parameters are chosen according to [31]. As remark, the work [31] was focused on simulation with hydrodynamic in the ideal mode and our work focuses on simulation with the relativistic hydrodynamics code vHLLE which includes viscous corrections. The initial parameters for vHLLE (for both energies) are the following: the transition from the initial state to the fluid dynamic description, or hydronynamization, takes place at $\tau = \tau_0 = 0.6$ fm/c. The transition from hydrodynamic fields to particles (hadrons) takes place at the hypersurface of fixed energy density $\epsilon_{sw} = 0.515$ GeV/fm^3. The shear viscosity to entropy density ratio is sat as $\eta/s = 0.15$ and bulk viscosity to entropy density is set $\zeta/s = 0.00$, although the hydrodynamic code is capable to evolve the bulk pressure as well. Since we used a visouc hydrodynamic model, we had to find new normalization parameters **n** for both energies. Our choice of normalisation parameters is shown in Table 4.1. The relation between the impact parameter and centrality for both energies is in Table 4.2, taken from [4]. The Trento3d model was used to generate 400 initial conditions. Each of these initial conditions is evolved once with vHLLE up until hadronisation. Then the hadronic system is sampled and evolved with SMASH 400 times, in order to increase statistics in a more economic way, because vHLLE simulations are very CPU demanding. Thus a single initial condition gives rise to 400 events. This procedure we call oversampling. This should guarantee sufficient statistics.

$\sqrt{s_{NN}}$[TeV]	**p**[-]	**k**[-]	**m**[-]	**w**[-]	**n**[-]	μ_0[-]	σ_0[-]	γ_0[-]	skewness	J[-]
2.76	0.0	2.0	6.0	0.59	114.0	0.0	2.9	7.3	1.0	0.75
5.02	0.0	2.0	6.0	0.59	135.0	0.0	2.9	7.3	1.0	0.75

Table 4.1: The initial condition parameters for Trento3d. Parametres taken from [31].

	$\sqrt{s_{NN}} = 2.76$ TeV		$\sqrt{s_{NN}} = 5.02$ TeV	
centrality	b_{min}	b_{max}	b_{min}	b_{max}
0–5%	0	3.47	0	3.49
5–10%	3.47	4.91	3.49	4.93
10–15%	4.91	6.01	4.93	6.04
15–20%	6.01	6.94	6.04	6.98
20–25%	6.94	7.76	6.98	7.8
25–30%	7.76	8.5	7.8	8.55
30–35%	8.5	9.18	8.55	9.23
35–40%	9.18	9.81	9.23	9.87
40–45%	9.81	10.4	9.87	10.5
45–50%	10.4	11	10.5	11
50–55%	11	11.5	11	11.6
55–60%	11.5	12	11.6	12.1
60–65%	12	12.5	12.1	12.6
65–70%	12.5	13	12.6	13.1
70–75%	13	13.4	13.1	13.5

Table 4.2: The impact parameters and centrality classes for Pb–Pb collisions at $\sqrt{s_{NN}} = 2.76$ TeV and $\sqrt{s_{NN}} = 5.02$ TeV. Parameters are taken form [35].

One typical example of the initial energy density distributions in the transverse plane at midrapidity for one event is presented in Fig. 4.1. There can be seen fluctuations in the initial state.

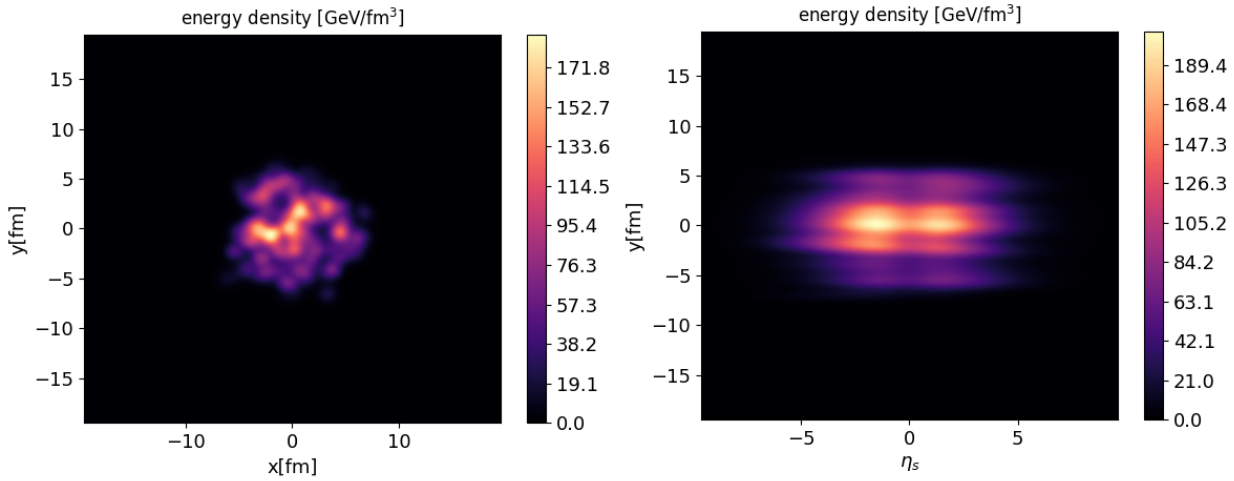

Figure 4.1: An example of a fluctuating (single event) initial energy density profile in the transverse plane at $\eta = 0$ (left) and $x = 0$ (right) corresponding to a centrality 0-5% Pb-Pb collision at $\sqrt{s_{NN}} = 5.02$ TeV.

4.1.1 Distribution of charged hadrons in pseudorapidity

We will start with the most basic observable model-wise: the pseudorapidity density of charged hadrons.

In the paper [3] the first wide-range measurement of the charged-particle pseudorapidity density distribution, for different centralities in Pb-Pb collisions at $\sqrt{s_{NN}} = 2.76$ TeV at the LHC was published. The measurement is performed using the full coverage of the ALICE detectors, $-5.0 < \eta < 5.5$, and employing a special analysis technique based on collisions arising from LHC satellite bunches.

The experimental data for charged-particle pseudorapidity density in Pb–Pb collisions at $\sqrt{s_{NN}} = 5.02$ TeV can be found in [10]. The measurement covers a wide pseudorapidity range from $-3.5 < \eta < 5$, which is sufficient for reliable estimates of the total number of charged particles produced in the collisions.

As we can see, Figure 4.2 and Figure 4.3 show behaviour of rapidity distribution of charge particles and pseudorapitity distribution of charge particles at $\sqrt{s_{NN}} = 2.76$ TeV and $\sqrt{s_{NN}} = 5.02$ TeV respectiverly for all available centrality classes. We can see that we have good agreement with data in range $-3.5 < \eta < 3.5$. In this range the hydrodynamics simulations describe data very well. In central collisions at $\sqrt{s_{NN}} = 5.02$ TeV our results and experimental data differ. It seems like we need little bit less particles in central collisions. But still the results from hydrodynamic simulations are sufficiently good. All centrality classes have been simulated with same parameters.

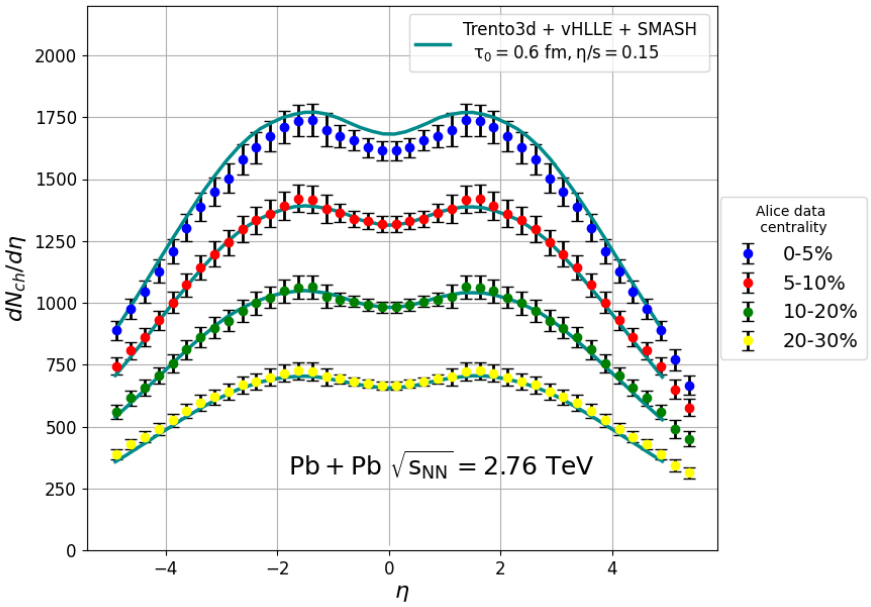

Figure 4.2: Charged–particle pseudorapidity density $dN/d\eta$ for four centrality classes in Pb–Pb collisions at $\sqrt{s_{NN}}$ = 2.76 TeV from the Trento3d+vHLLE+SMASH, compared with the experimental data taken from [3].

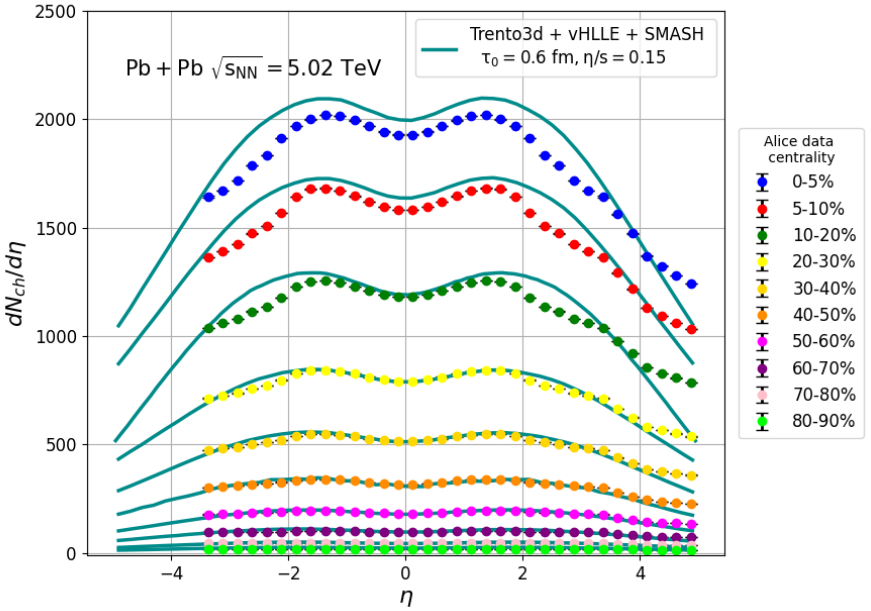

Figure 4.3: Charged–particle pseudorapidity density $dN/d\eta$ for ten centrality classes in Pb–Pb collisions at $\sqrt{s_{NN}}$ = 5.02 TeV from the Trento3d+vHLLE+SMASH, compared with the experimental data taken from [10].

4.1.2 Transverse momenta spectra

Let us first mention several phenomena concerning the transverse momenta spectra. The transverse momenta spectra can be divided into two parts - soft and hard. At the lower transverse momentum p_t, there is a soft part of the spectrum. These hadrons are genuinely producing non-perturbative processes. The hard part, which is described by the perturbative QCD, is at higher p_t. The hard part of the spectra usually contain for example jets.

For the transverse momentum spectra of hadrons the results from ALICE are taken. The spectra are presented in [5] for $\sqrt{s_{NN}} = 2.76$ TeV and [8] for $\sqrt{s_{NN}} = 5.02$ TeV, together with other bulk properties for different centralities and various collision energies.

In [5] measurements are presented of pions $\pi^{\pm}$, kaons $K^{\pm}$, protons p and antiprotons $\bar{p}$ production at mid-rapidity ($|y| < 0.5$), in Pb–Pb collisions at $\sqrt{s_{NN}} = 2.76$ TeV as a function of centrality. The measurement covers the transverse momentum p_T range from $100, 200, 300$ MeV/c up to $3, 3, 4.6$ GeV/c, for $\pi^{\pm}$, $K^{\pm}$, and p.

In [8] mid-rapidity production of $\pi^{\pm}$, $K^{\pm}$, p and $\bar{p}$ is measured by the ALICE experiment at the LHC, in Pb-Pb and inelastic pp collisions at $\sqrt{s_{NN}} = 5.02$ TeV is shown. The invariant yields are measured over a wide transverse momentum p_t range from hundreds of MeV/c up to 20 GeV/c. The results in Pb-Pb collisions are presented as a function of the collision centrality, in the range 0-90%.

In Figures 4.4, 4.5, 4.6 and 4.6 we can see the transverse momentum spectra of charged hadrons: π^+, K^+, p, π^-, $\bar{p}$ and K^- at $\sqrt{s_{NN}} = 2.76$ TeV for ten centrality classes. The results from hydrodynamic simulations are compared with experimental data from ALICE. The experimental data were measured up to 4.6 GeV in p_t. In higher p_t about 3 GeV some hard processes occur. The hydrodynamic simulations can not describe these processes. We have good agreement with data up to 2.0 GeV. We have the best results for the pions because the pions are the most represented. In peripheral collisions, for example centrality 80-90%, we do not have good results. We can see some statistical fluctuations. The reason is simple. In peripheral collisions, the overlap of two nuclei is not large, so hydrodynamic evolution is not strong. In central collisions, we have good agreement. We can see it in Figures 4.7 and 4.8. These two figures represent an example of transverse momentum spectra for the centrality class 10-20%.

In Figures 4.9, 4.10 and 4.11 transverse momentum spectra of $\pi^{\pm}$, $K^{\pm}$, $\bar{p}$ and p at $\sqrt{s_{NN}} = 5.02$ TeV from simulations are depicted. Like in the case of energy $\sqrt{s_{NN}} = 2.76$ TeV also for this case, we have agreement with data up to 3.5 GeV in p_t. Higher p_t, our results do not describe data properly, because of hard processes.

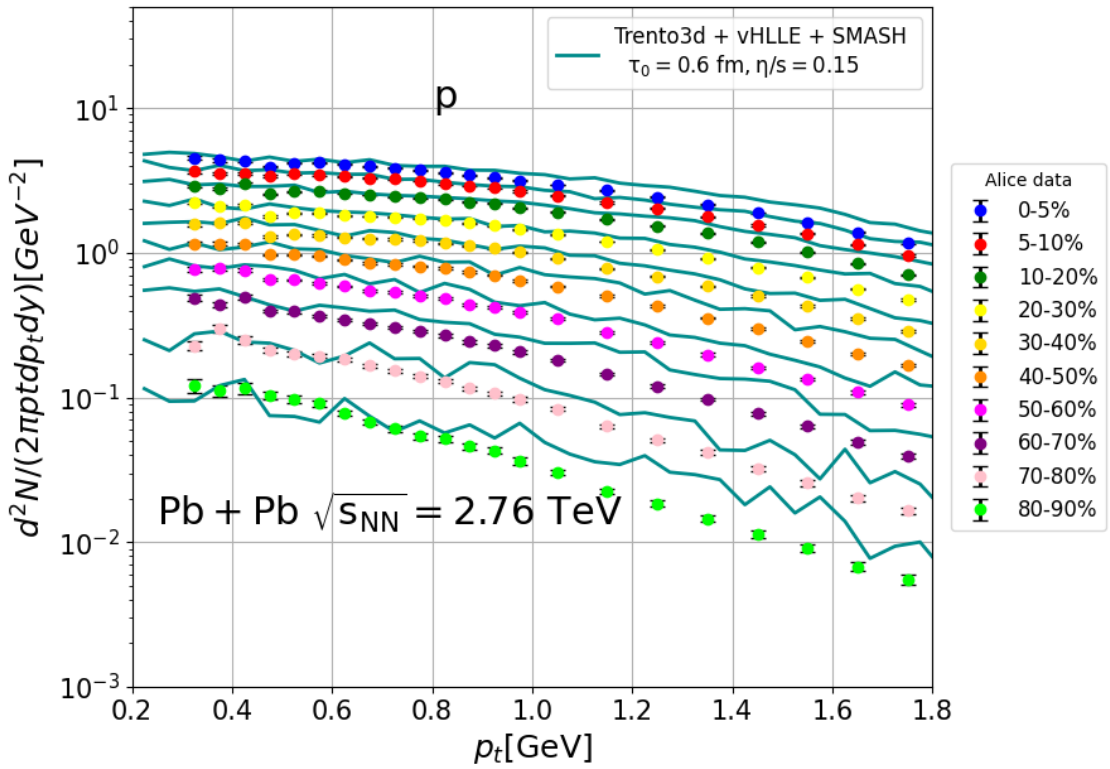

Figure 4.4: Transverse momentum spectra of protons for ten centrality classes in Pb–Pb collisions at $\sqrt{s_{NN}} = 2.76$ TeV from the Trento3d+vHLLE+SMASH, compared with the experimental data taken from [5].

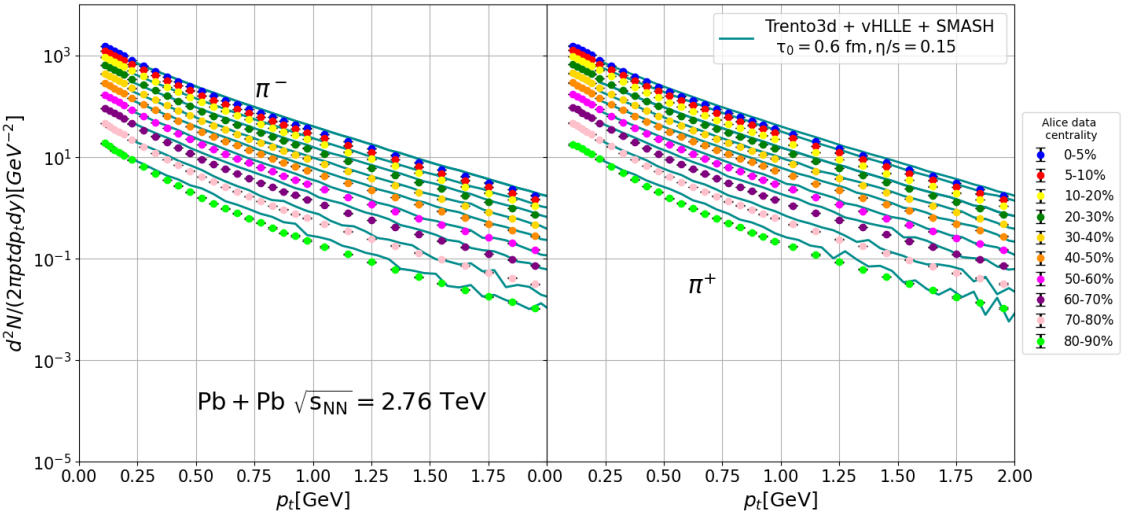

Figure 4.5: Transverse momentum spectra of π^- and π^+ for ten centrality classes in Pb–Pb collisions at $\sqrt{s_{NN}} = 2.76$ TeV from the Trento3d+vHLLE+SMASH, compared with the experimental data taken from [5].

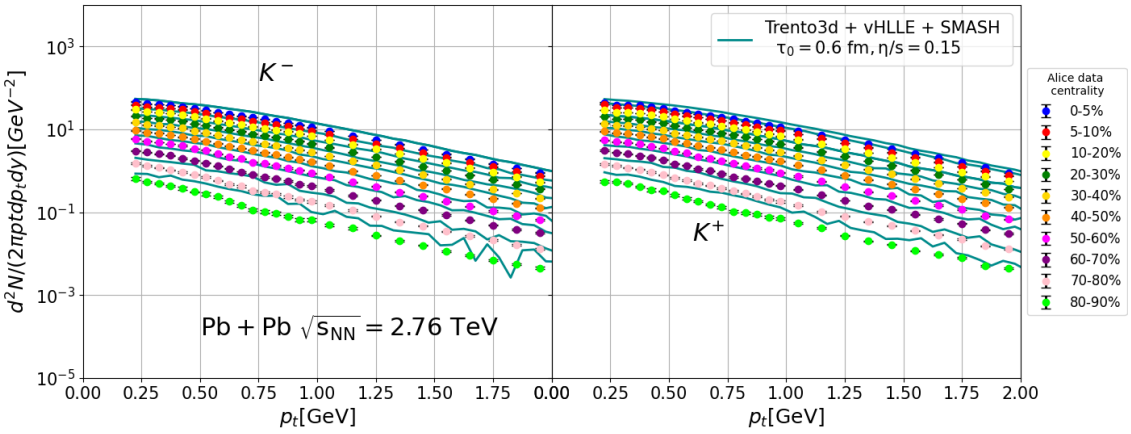

Figure 4.6: Transverse momentum spectra of K^- and K^+ for ten centrality classes in Pb–Pb collisions at $\sqrt{s_{NN}} = 2.76$ TeV from the Trento3d+vHLLE+SMASH, compared with the experimental data taken from [5].

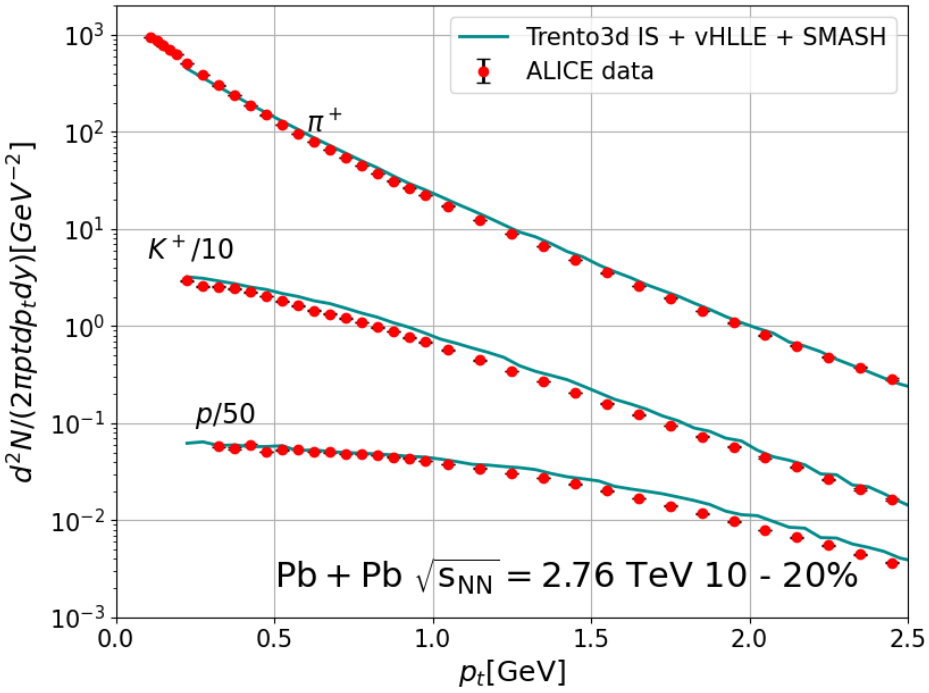

Figure 4.7: Transverse momentum spectra of π^+, K^+ and p in collisions Pb+Pb at $\sqrt{s_{NN}} = 2.76$ TeV for centrality 10-20% from the Trento3d+vHLLE+SMASH. Experimental data are taken from [5].

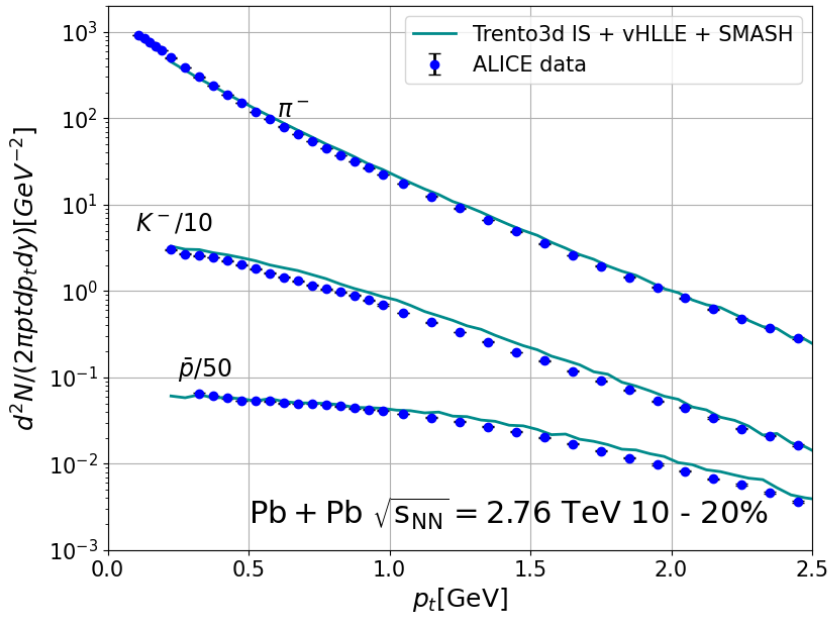

Figure 4.8: Transverse momentum spectra of π^-, K^- and $\bar{p}$ in collisions Pb+Pb at $\sqrt{s_{NN}}$ = 2.76 TeV for centrality 10-20% from the Trento3d+vHLLE+SMASH. Experimental data are taken from [5].

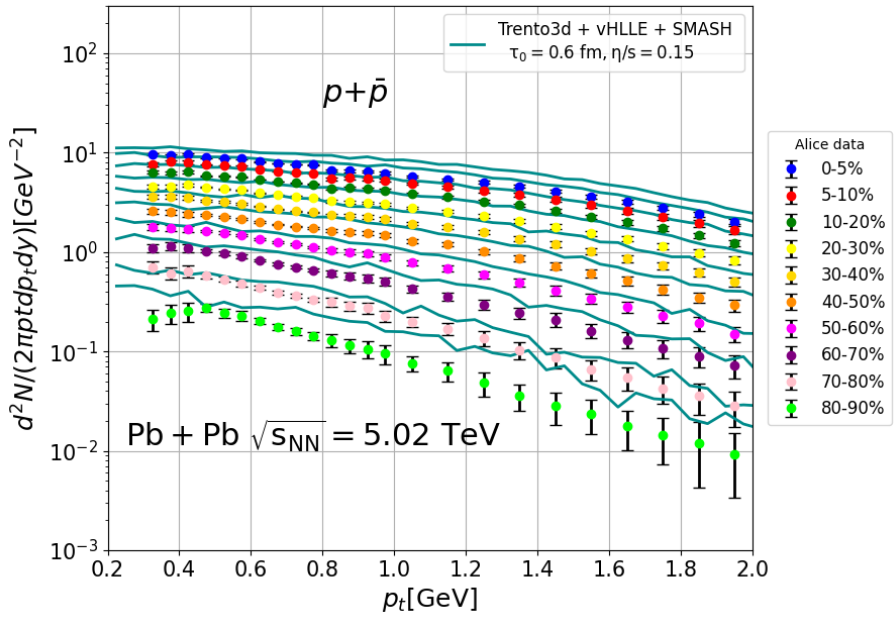

Figure 4.9: Transverse momenta spectrum of p and $\bar{p}$ for ten centrality classes in Pb–Pb collisions at $\sqrt{s_{NN}}$ = 5.02 TeV from the Trento3d+vHLLE+SMASH, compared with the experimental data taken from [8].

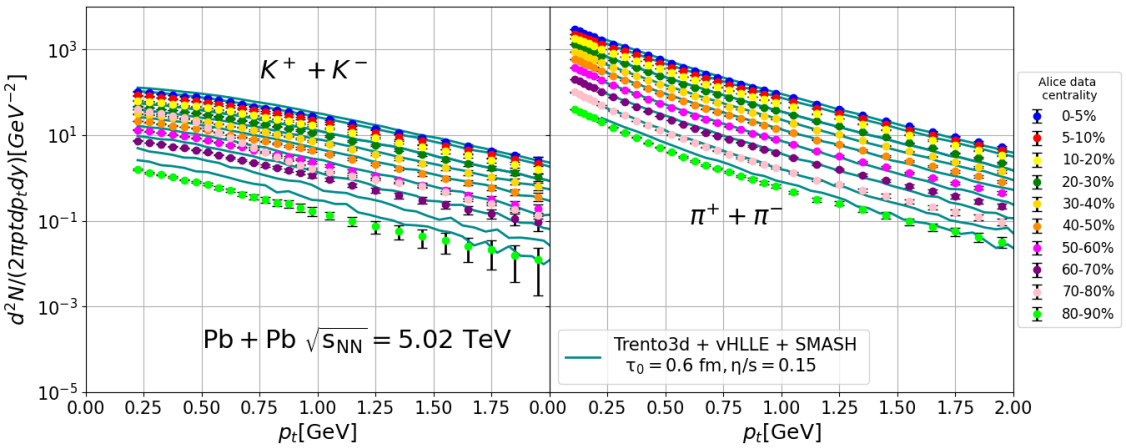

Figure 4.10: Transverse momentum spectra of $\pi^{\pm}$ and $K^{\pm}$ for ten centrality classes in Pb–Pb collisions at $\sqrt{s_{NN}}$ = 5.02 TeV from the Trento3d+vHLLE+SMASH, compared with the experimental data taken from [8].

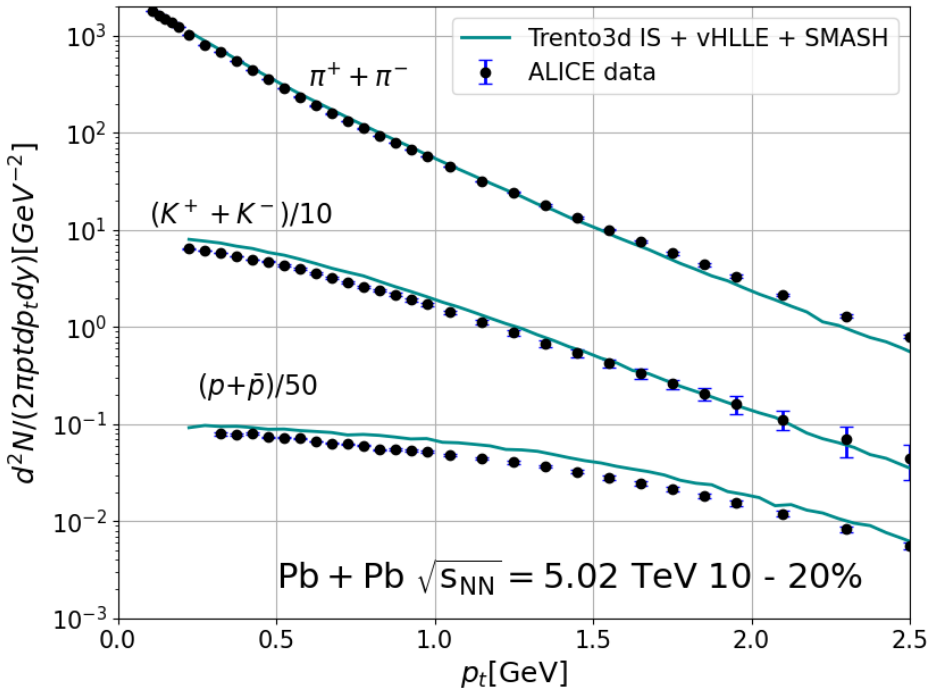

Figure 4.11: Transverse momentum spectra of $\pi^{\pm}$, $K^{\pm}$, $\bar{p}$ and p in collisions Pb+Pb at $\sqrt{s_{NN}}$ = 5.02 TeV for centrality 10-20% from the Trento3d+vHLLE+SMASH. Experimental data are taken from [8].

4.1.3 Elliptic flow v_2

The next observable, which can be computed and compared with data, is the elliptic flow v_2.

The experimental data [6] for the elliptic flow coefficient v_2 of identified hadrons in Pb–Pb collisions at $\sqrt{s_{NN}} = 2.76$ TeV were measured with the ALICE detector at the LHC. The results were obtained with two-particle correlation technique, using a pseudo-rapidity gap of $|\Delta\eta| > 0.9$ between the identified hadrons under study and the reference particles. The v_2 is reported for $\pi^{\pm}$, $K^{\pm}$, $\bar{p}$ and p in several collision centralities.

The data set of the elliptic v_2, triangular v_3, and quadrangular v_4 flow coefficients of $\pi^{\pm}$, $K^{\pm}$, $\bar{p}$ and p in Pb–Pb collisions at $\sqrt{s_{NN}} = 5.02$ TeV was published in [7]. Results obtained with the scalar product method are reported for the rapidity range $|y| < 0.5$ as a function of transverse momentum, p_t, at different collision centrality intervals between 0–70%, including ultra-central (0–1%) collisions. For $p_t < 3$ GeV/c, the flow coefficients exhibit a particle mass dependence.

In Figures 4.12 and 4.13, the elliptic flow v_2 calculated with 2-particle cumulant as function of centrality is depicted for both energies. In particular, the elliptic flow coefficient is observed to increase with increasing centrality, indicating a stronger collective behaviour of the produced matter in more central collisions.

In Figures 4.14 and 4.16 the flow coefficient $v_2\{2\}$ as a function of p_t of $\pi^{\pm}$ and $K^{\pm}$ is depicted. Figure 4.14 shows the flow coefficient $v_2\{2\}$ as a function of p_t for $K^{\pm}$ and $\pi^{\pm}$ at $\sqrt{s_{NN}} = 2.76$ TeV for four different centrality classes, computed as the two-particle cumulats (1.18). Figure shows 4.14 the flow coefficient $v_2\{2\}$ for the centrality 10-20%.

Firstly, we see that the $v_2\{2\}$ grows with increasing p_t and decreasing centrality. Secondly, our results from hydrodynamic simulations describe the experimental data very well. Nevertheless, in all figures with the two-particle cumulats $v_2\{2\}$ non-monotonic behaviour are visible in increasing p_t. These irregularities are caused by the statistical fluctuations.

In Figure 4.15 and 4.17 the $v_2\{2\}$ as a function of p_t for $\pi^{\pm}$ and $K^{\pm}$ at $\sqrt{s_{NN}} = 5.02$ TeV is plotted. Figure 4.17 shows the $v_2\{2\}$ as a function of p_t for the centrality 10-20%. Our simulation describes data very well. For the kaons, we have good agreement with data up to 2.5 GeV in p_t. We can see the statistical irregularities again. Our simulations had 160000 events. All figures, which include the elliptic flow, don't show statistical error intervals because we have had problems with the calculations. But if we plotted them, we would see big statistical fluctuation.

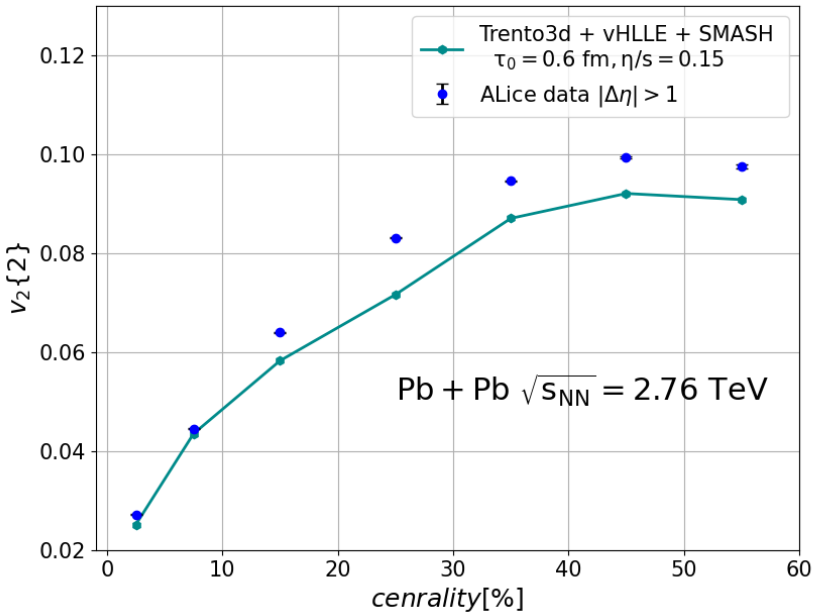

Figure 4.12: The elliptic flow $v_2\{2\}$ of the charged hadrons as a function of *centrality* in collisions Pb+Pb at $\sqrt{s_{NN}} = 2.76$ TeV from simulations with Trento3d+vHLLE+SMASH. Experimental data are taken from [9].

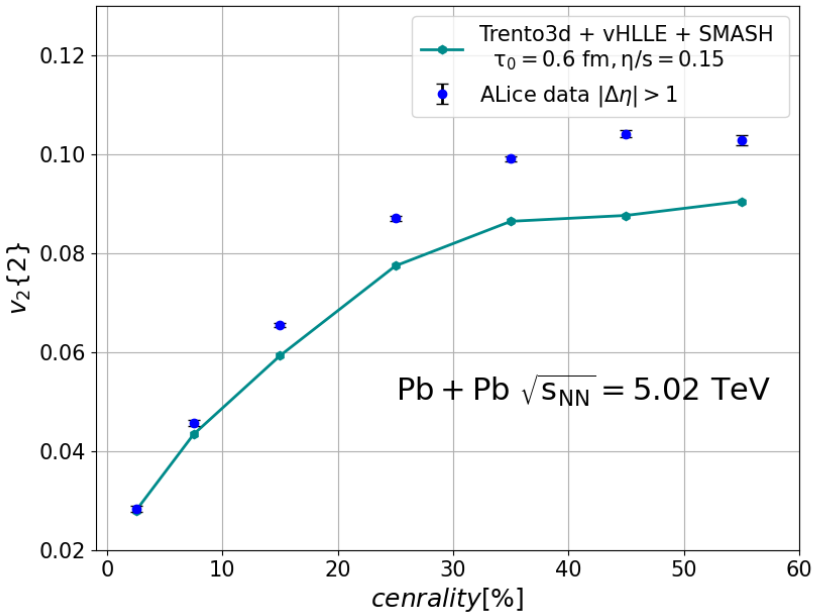

Figure 4.13: The elliptic flow $v_2\{2\}$ of the charged hadrons as a function of *centrality* in collisions Pb+Pb at $\sqrt{s_{NN}} = 5.02$ TeV from simulations with Trento3d+vHLLE+SMASH. Experimental data are taken from [9].

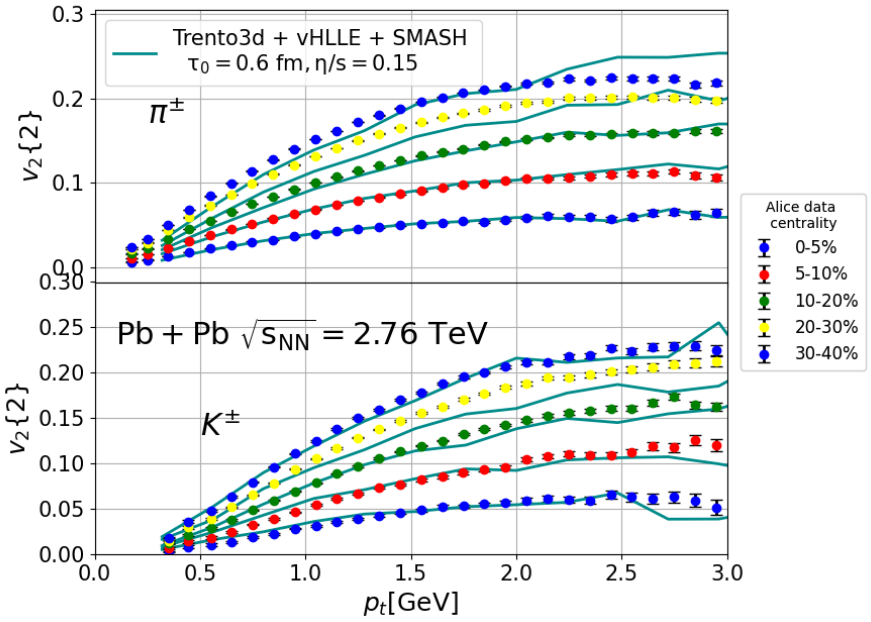

Figure 4.14: The elliptic flow $v_2\{2\}$ as a function of p_t a spectra of $\pi^{\pm}$ and $K^{\pm}$ in collisions Pb+Pb at $\sqrt{s_{NN}} = 2.76$ TeV for four centrality classes from simulations with Trento3d+vHLLE+SMASH. Experimental data are taken from [6].

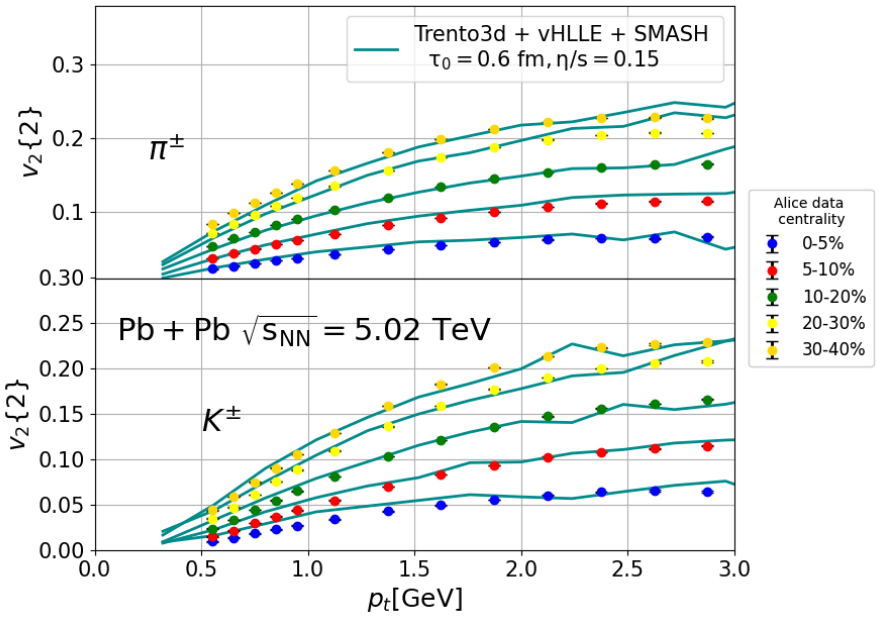

Figure 4.15: The elliptic flow $v_2\{2\}$ as a function of p_t a spectra of $\pi^{\pm}$ and $K^{\pm}$ in collisions Pb+Pb at $\sqrt{s_{NN}} = 5.02$ TeV for four centrality classes from simulations with Trento3d+vHLLE+SMASH. Experimental data are taken from [7].

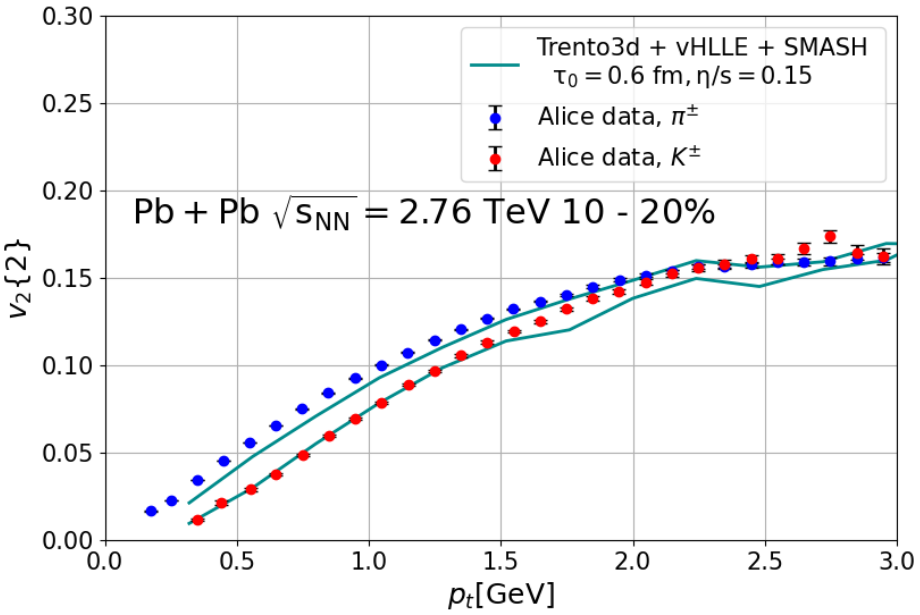

Figure 4.16: The elliptic flow $v_2\{2\}$ as a function of p_t a spectra of $\pi^{\pm}$ and $K^{\pm}$ in collisions Pb+Pb at $\sqrt{s_{NN}} = 2.76$ TeV for centrality 10-20% from simulation with Trento3d+vHLLE+SMASH. Experimental data are taken from [6].

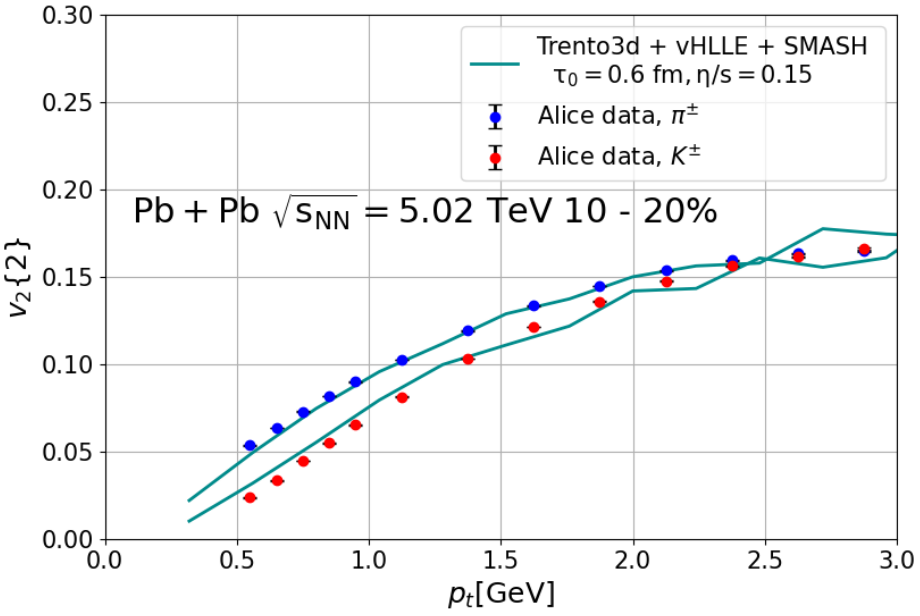

Figure 4.17: The elliptic flow $v_2\{2\}$ as a function of p_t a spectra of $\pi^{\pm}$ and $K^{\pm}$ in collisions Pb+Pb at $\sqrt{s_{NN}} = 5.02$ TeV for centrality 10-20% from simulation with Trento3d+vHLLE+SMASH. Experimental data are taken from [7].

4.1.4 Elliptic flow v_2 fluctuations

The main goal of this master thesis is to investigate fluctuations occurring at LHC energies, specifically focusing on event-by-event elliptic flow v_2 fluctuations in heavy-ion collisions. These fluctuations serve as direct indicators of the fluctuating geometry of the quark-gluon plasma and are highly sensitive to any deviations from spherical symmetry in the colliding nuclei shapes. This chapter concentrates on event-by-event fluctuations.

Figure 4.18 shows the event-by-event elliptic flow fluctuations δv_2 (computed from (1.7)) plotted as a function of centrality for Pb-Pb collisions at $\sqrt{s_{NN}} = 2.76$ TeV and $\sqrt{s_{NN}} = 5.02$ TeV, computed using Event Plane Method (1.15) and (1.7) with Trento3d+vHLLE+SMASH. The plot demonstrates that the fluctuations increase with higher centrality, which corresponds to the fact that elliptic flow also increases with centrality, as illustrated in Figures 4.12 and 4.13. It is not surprising that fluctuations are dominant at less central collisions.

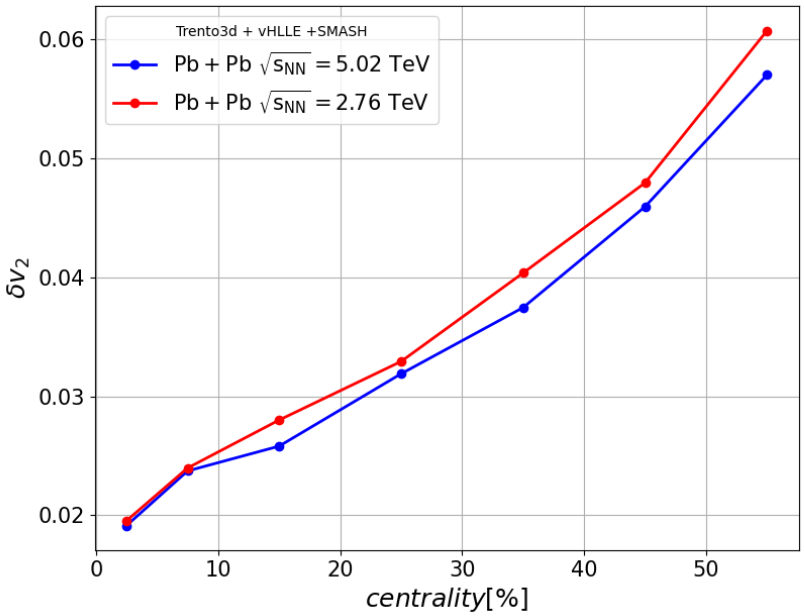

Figure 4.18: Elliptic flow fluctuations event by event δv_2 as function of centrality Pb-Pb at $\sqrt{s_{NN}} = 2.76$ TeV (red line) and $\sqrt{s_{NN}} = 5.02$ TeV for Trento3d+vHLLE+SMASH.

Figure 4.19 illustrates the elliptic flow fluctuation as a function of transverse momentum p_t for six centrality classes at two investigated energies $\sqrt{s_{NN}} = 2.76$ TeV and $\sqrt{s_{NN}} = 5.02$ TeV. The elliptic flow fluctuation δv_2 is a measurement of the event-by-event variation in the elliptic flow v_2 of the produced particles.

As p_t increases, we observe a rapid increase of δv_2, indicating that the flow fluctuations become large at high p_t. Specifically, for p_t values in the range of $(2.0, 2.9)$ GeV,

the δv_2 values are higher than the v_2 values, which means that in some events high p_t.

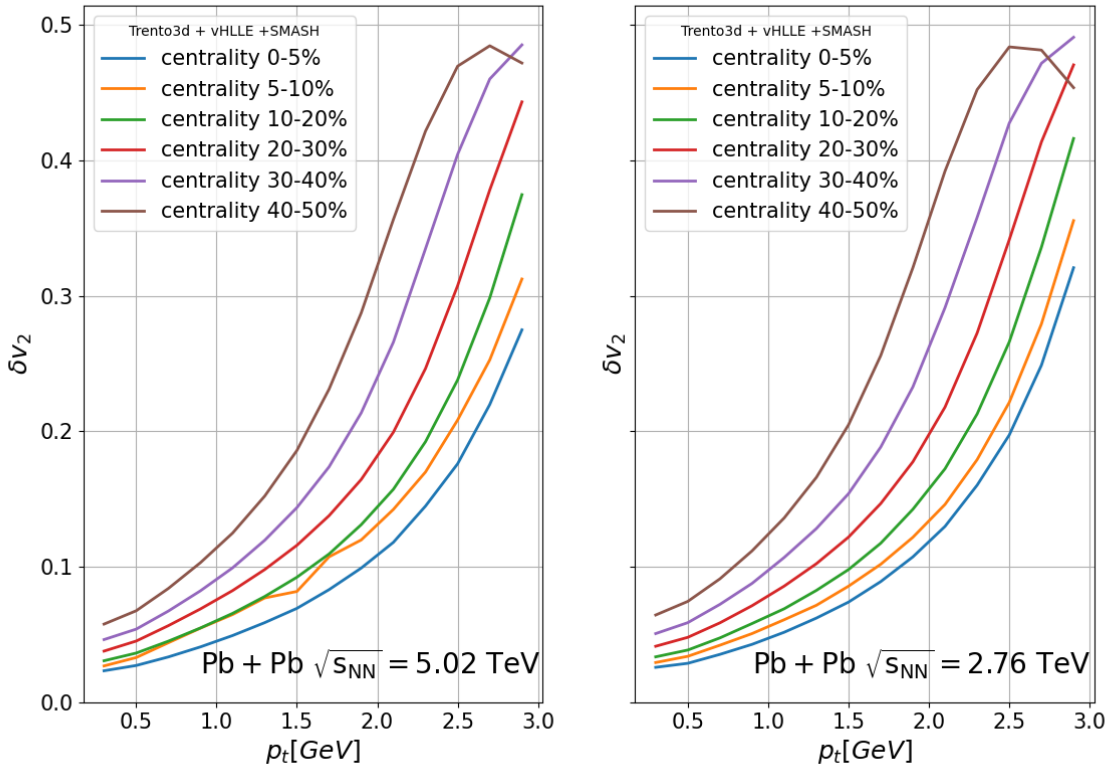

Figure 4.19: Elliptic flow event by event fluctuations δv_2 as function of p_t at $\sqrt{s_{NN}}$ = 2.76 TeV (right) and $\sqrt{s_{NN}} = 5.02$ TeV (left) for Trento3d+vHLLE+SMASH.

Therefore, we explore the event-by-event distribution of v2 and show them in Figures 4.20, 4.21, 4.22 and 4.23 depict the distribution dN/dv_2 of elliptic flow v_2 in events using Trento3d+vHLLE+SMASH hybrid model at a collision energy of $\sqrt{s_{NN}} = 2.76$ TeV and $\sqrt{s_{NN}} = 5.02$ TeV for centralities 10-20% and 40-50%. The distributions are shown for three different values of transverse momentum p_t, namely 0.5 GeV, 2.3 GeV and 2.9 GeV.

At lower $p_t = 0.5$ GeV values, as shown in the left side of the Figures 4.20, 4.21, 4.22 and 4.23, the dN/dv_2 is distributed according to narrow bell-shaped distribution around the mean value $< v_2 >$ of elliptic flow with the width $(\delta v_2)^2$. At higher p_t values, as shown in the right side of above mention figures, the v_2 distribution becomes flatter and peaks close to zero. It leads to fact that negative v_2 contributes to the mean value of v_2. The negative v_2 values signify that the particles are preferentially emitted in the perpendicular direction, normally to the direction of the initial collisional geometry. This behaviour could be attributed to the dominance of jet production at high p_t, which reduces the contribution of elliptic flow to the overall particle distribution. When v_2 is negative, it means that the event plane in

the corresponding bin p_t should be oriented differently than the global event plane. The new results show that we have fluctuations not only in the magnitude of the elliptical flow, but also in the direction of the event plane, if the plane were determined from event to event. This is a good motivation for the analysis as suggested by [40, 41].

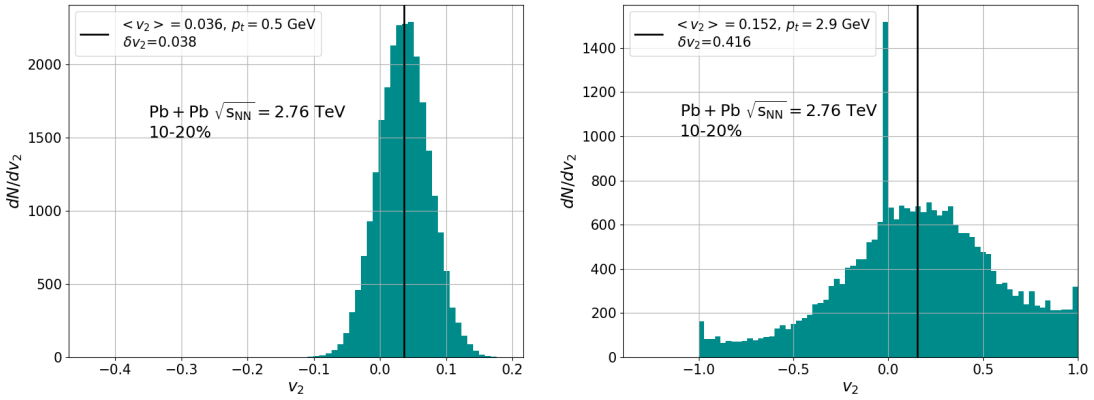

Figure 4.20: Distribution dN/dv_2 of elliptic flow v_2 in events from Trento3d+vHLLE+SMASH for $p_t = 0.5$ GeV (left) and $p_t = 2.9$ GeV (right) at $\sqrt{s_{NN}} = 2.76$ TeV for centrality 10-20%.

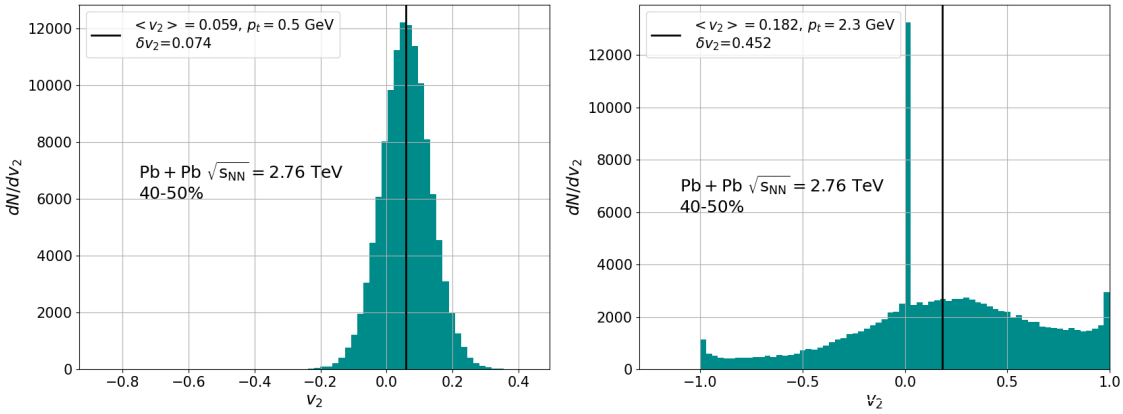

Figure 4.21: Distribution dN/dv_2 of elliptic flow v_2 in events from Trento3d+vHLLE+SMASH for $p_t = 0.5$ GeV (left) and $p_t = 2.3$ GeV (right) at $\sqrt{s_{NN}} = 2.76$ TeV for centrality 40-50%.

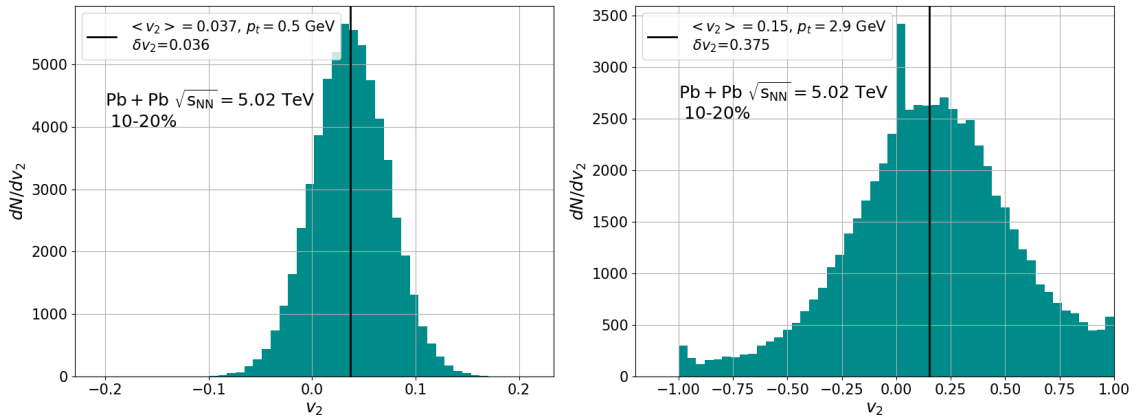

Figure 4.22: Distribution dN/dv_2 of elliptic flow v_2 in events from Trento3d+vHLLE+SMASH for p_t = 0.5 GeV (left) and p_t = 2.9 GeV (right) at $\sqrt{s_{NN}}$ = 5.02 TeV for centrality 10-20%.

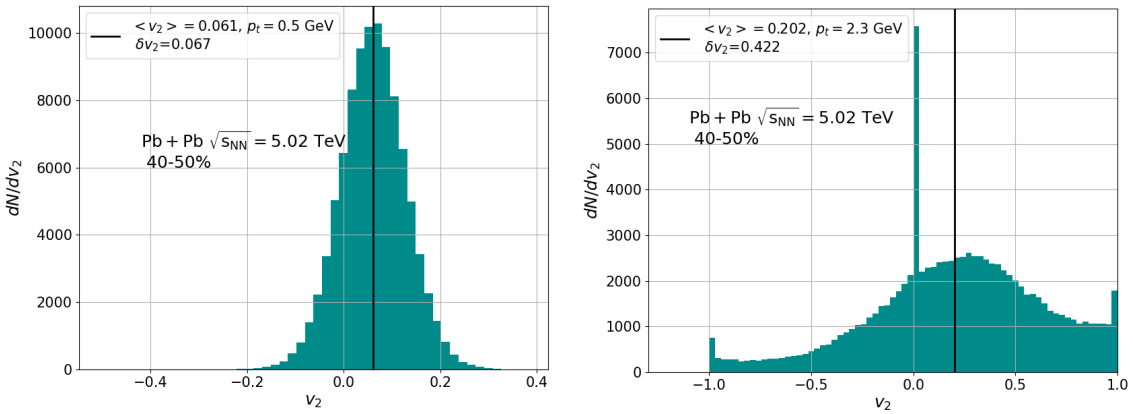

Figure 4.23: Distribution dN/dv_2 of elliptic flow v_2 in events from Trento3d+vHLLE+SMASH for p_t = 0.5 GeV (left) and p_t = 2.3 GeV (right) at $\sqrt{s_{NN}}$ = 5.02 TeV for centrality 10-20%.

4.2 Simulation with Trento

The initial parameters for Trento are shown in Table 4.3 for both energies. The parameters in Table 4.3 are discussed in Chapter 3. The parameter σ_{NN} for the energy $\sqrt{s_{NN}} = 2.76$ TeV is taken from [1] and for the energy $\sqrt{s_{NN}} = 5.02$ TeV from [8]. The relation between impact parameter and centrality for both energies is taken from [4]. Parameters **p**, **k**, **d**, **m**, **w** and **v** are taken from [38]. Number of events **N** for the Trento model is 100. In total, we have 100×100 events.

$\sqrt{s_{NN}}$ [TeV]	σ_{NN} [fm^2]	b_{min} [fm]	b_{max} [fm]	**p** [−]	**k** [−]	**d** [fm]	**m** [−]	**w** [fm]	**v** [fm]
2.76	6.4	6.98	8.55	0	1	1.27	6	0.98	0.43
5.02	7.0	6.98	8.55	0	1	1.27	6	0.98	0.43

Table 4.3: The initial Trento parameters for hydrodynamic simulation. Parameters are taken from [38].

We previously encountered a normalization issue with our extension into the η_s and addressed it by upgrading the initial state for Trento2d in vHLLE. We then compared the charged hadrons distribution in pseudorapidity from simulations with Trento2d and Trento3d for the 10-20% centrality class and both energies, as shown in Figures 4.24 and 4.25. Our upgrade of Trento2d in vHLLE resolved the normalization issue and works well for all centrality classes, although Trento3d more accurately describes experimental data.

Furthermore, we compared the transverse momentum spectra of charged hadrons from simulations with Trento2d and Trento3d for the 10-20% centrality class and both energies, as depicted in Figures 4.26, 4.27, and 4.28. We observed that Trento3d produces better results than Trento2d, with more transverse flow. However, we still consider the results from Trento2d to be reliable.

In Figures 4.29 and 4.30 are depicted the flow coefficient $v_2\{2\}$ as a function of p_t of $\pi^{\pm}$ and $K^{\pm}$ at $\sqrt{s_{NN}} = 2.76$ TeV and $\sqrt{s_{NN}} = 5.02$ TeV for centrality 10-20%.

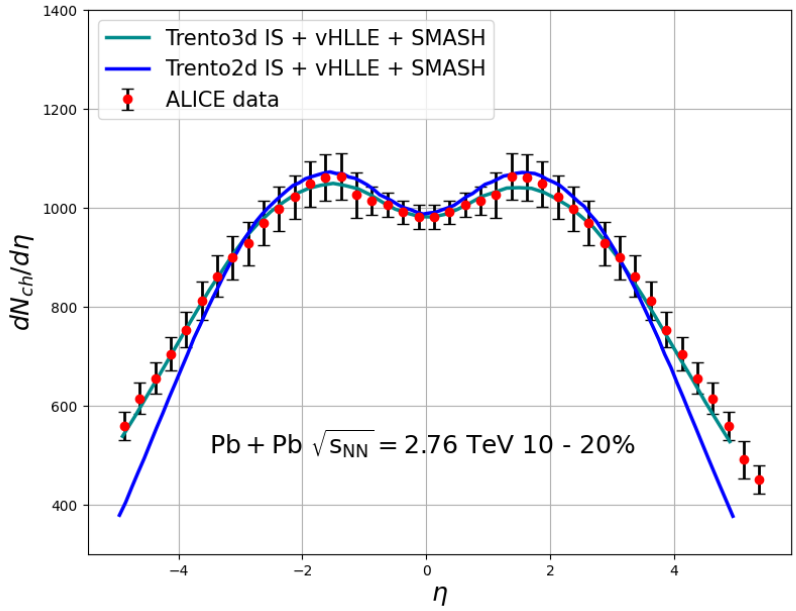

Figure 4.24: Charged–particle pseudorapidity density $dN/d\eta$ in collisions Pb-Pb at $\sqrt{s_{NN}}$ = 2.76 TeV for centrality 10-20% from the Trento+vHLLE+SMASH and Trento3d+vHLLE+SMASH, compared with the experimental data taken from [3].

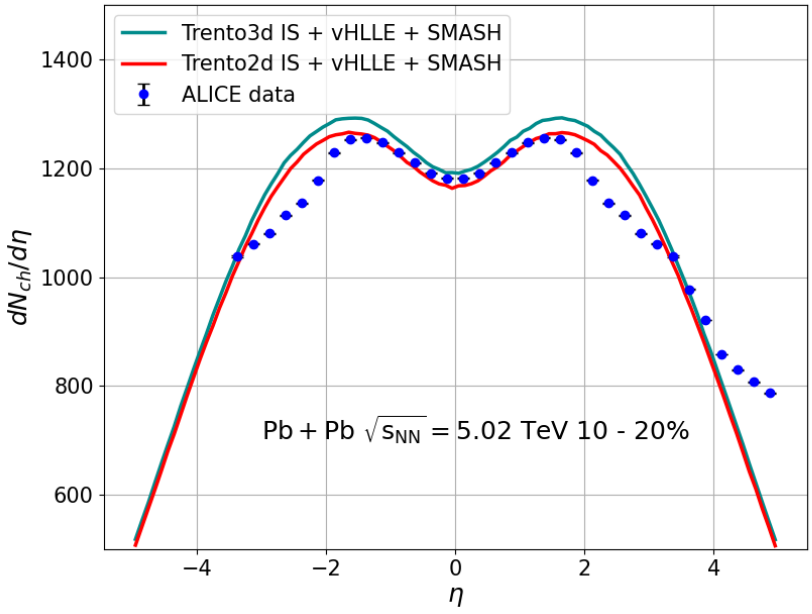

Figure 4.25: Charged–particle pseudorapidity density $dN/d\eta$ for charged particles in collisions Pb-Pb at $\sqrt{s_{NN}}$ = 5.02 TeV for centrality 10-20% from the Trento+vHLLE+SMASH and Trento3d+vHLLE+SMASH, compared with the experimental data taken from [10].

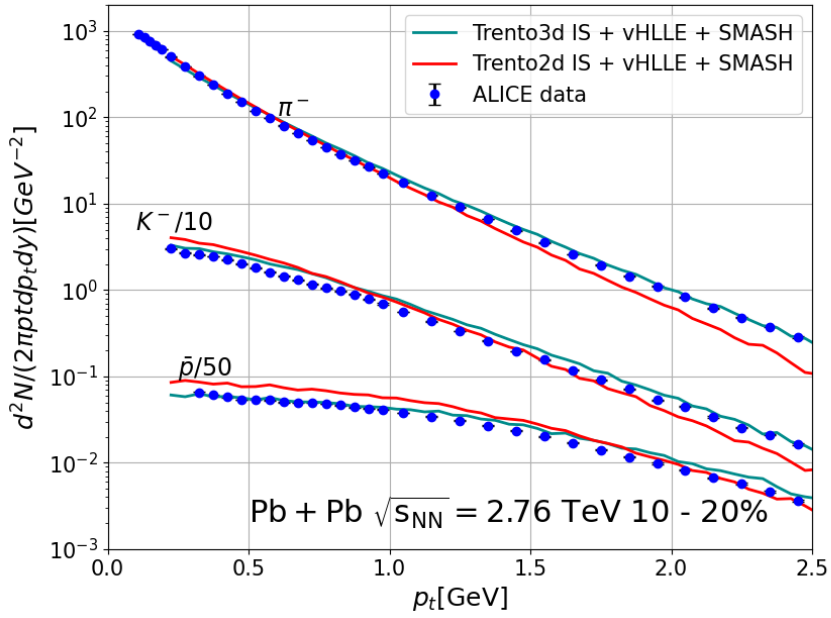

Figure 4.26: Transverse momentum spectra of π^-, K^- and $\bar{p}$ in collisions Pb+Pb at $\sqrt{s_{NN}} = 2.76$ TeV for centrality 10-20% from the Trento2d+vHLLE+SMASH and Trento3d+vHLLE+SMASH. Experimental data are taken from [5].

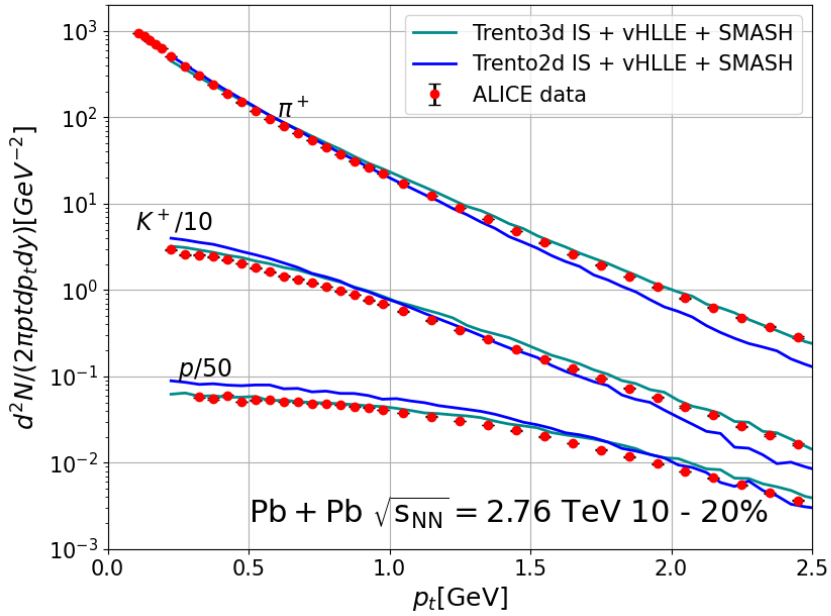

Figure 4.27: Transverse momentum spectra of π^+, K^+ and p in collisions Pb+Pb at $\sqrt{s_{NN}} = 2.76$ TeV for centrality 10-20% from the Trento2d+vHLLE+SMASH and Trento3d+vHLLE+SMASH. Experimental data are taken from [5].

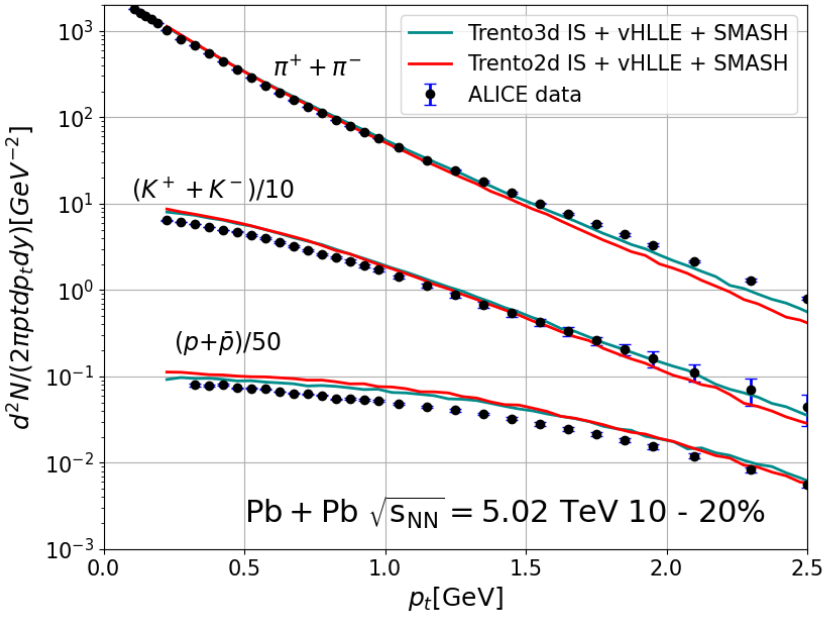

Figure 4.28: Transverse momentum spectra of $\pi^{\pm}$, $K^{\pm}$ and $p+\bar{p}$ in collisions Pb+Pb at $\sqrt{s_{NN}} = 5.02$ TeV for centrality 10-20% from the Trento2d+vHLLE+SMASH and Trento3d+vHLLE+SMASH. Experimental data are taken from [8].

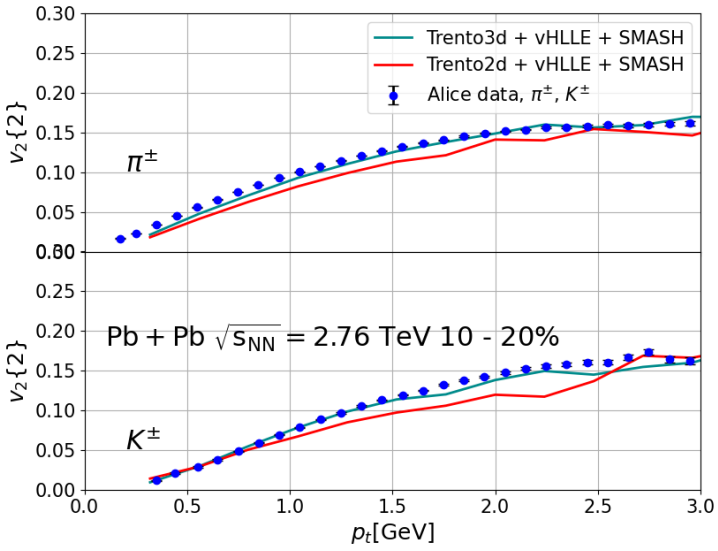

Figure 4.29: The elliptic flow $v_2\{2\}$ as a function of p_t a spectra of $\pi^{\pm}$ and $K^{\pm}$ in collisions Pb+Pb at $\sqrt{s_{NN}} = 2.76$ TeV for centrality 10-20% from the Trento2d+vHLLE+SMASH and Trento3d+vHLLE+SMASH. Experimental data are taken from [6].

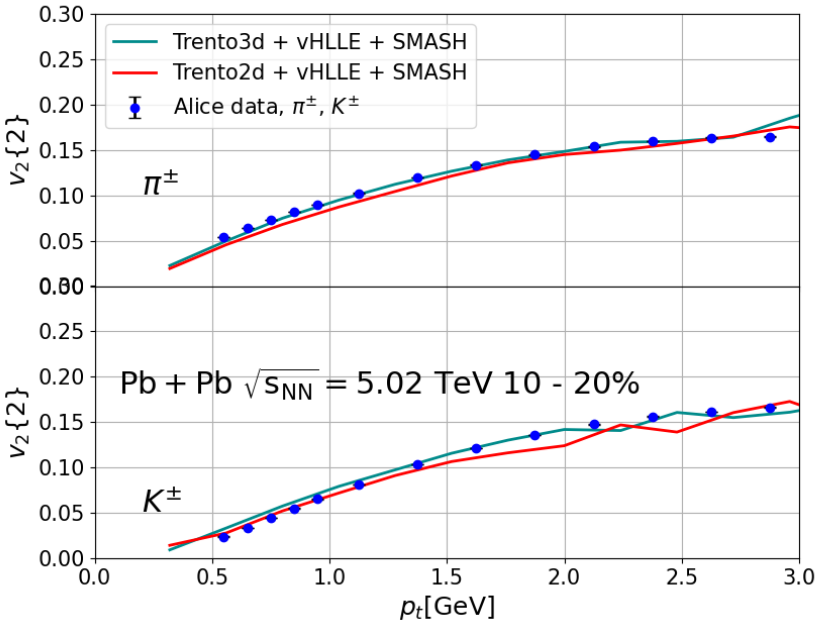

Figure 4.30: The elliptic flow $v_2\{2\}$ as a function of p_t a spectra of $\pi^{\pm}$ and $K^{\pm}$ in collisions Pb+Pb at $\sqrt{s_{NN}}$ = 5.02 TeV for centrality 10-20% from the Trento2d+vHLLE+SMASH and Trento3d+vHLLE+SMASH. Experimental data are taken from [8].

Conclusions

The main goal of this master thesis was to calibrate the hybrid hydrodynamic model for CERN LHC energies and to study a behaviour of elliptic flow, which is created immediately after the collision of two nuclei.

The first chapter contains the basic knowledge of heavy ion collisions and quark-gluon plasma creation. The space-time evolution of heavy ion collision is investigated, and the anisotropic flow that results from the hydrodynamic expansion is discussed. The flow is caused by the hydrodynamic expansion that begins just after the collision of two nuclei. The methods of flow measurement, namely event plane method and cumulant method, are mentioned and discussed in this chapter. The flow angle and flow magnitude fluctuations in Pb-Pb collisions are discussed in this chapter as well.

The second chapter focuses on the theory of relativistic hydrodynamics, including the ideal hydrodynamics that describes the dynamics of an ideal fluid. The relativistic Navier-Stokes equations, which describe the dynamics of a viscous fluid, are derived.

The last two chapters delve into hydrodynamic modeling in particle physics. The three-step process of initial state, hydrodynamic evolution, and transition from fluid to particles is explained. The hybrid hydrodynamic package used in this study consisted of Trento and Trento3d as the initial state model, vHLLE as the hydrodynamic model, and SMASH as the afterburner model. The choice of Trento and Trento3d as the initial state model was motivated by previous studies showing their suitability for LHC energies. The study specifically focused on Pb+Pb collisions at $\sqrt{s_{NN}} = 2.76$ TeV and $\sqrt{s_{NN}} = 5.02$ TeV.

In order to study the behaviour of elliptic flow namely the fluctuation in magnitude and its direction, it is necessary to perform the calibration of the hybrid package. To provide successful calibration, our data from simulations with the experimental data are compared.

The distributions of the pseudorapidity distributions of charged hadrons are shown in Figure 4.2 for $\sqrt{s_{NN}} = 2.76$ TeV and in Figure 4.3 for $\sqrt{s_{NN}} = 5.02$ TeV. It can be clearly seen that our results are consistent with experimental data in range $-4.5 < \eta < 4.5$ for $\sqrt{s_{NN}} = 2.76$ TeV and $-3.0 < \eta < 3.0$ for $\sqrt{s_{NN}} = 5.02$ TeV. In Figures 4.24 and 4.25, the comparison between Trento2d and Trento3d for pseudorapidity distributions of charged hadrons is shown. The Trento3d gives better results than Trento2d.

The results of our simulations for the spectrum of transverse momentum of charged

hadrons in the mid-rapidity for π^+, K^+, p, π^-, $\bar{p}$ and K^- have been computed and are presented in Figures 4.5, 4.6, **??** and 4.8 for the energy $\sqrt{s_{NN}} = 2.76$ TeV and Figures 4.9, 4.10 and 4.11 for $\sqrt{s_{NN}} = 5.02$ TeV. The results are compared with the experimental data and our simulations describe experimental data very well. In higher p_t our results does not describe data properly, because of hard processes. The hydrodynamic simulation can not describe these processes.

Last observable, which has been computed, is the elliptic flow of charged hadrons. In Figures 4.12 and 4.13, the coefficient $v_2\{2\}$ as function of centrality is depicted. The flow coefficient increases with decreasing centrality. On the other hand, the elliptic flow in very peripheral collisions is small. In Figure 4.14 and 4.16, $v_2\{2\}$ as function of transverse momentum for $\pi^{\pm}$ and $K^{\pm}$ at $\sqrt{s_{NN}} = 2.76$ TeV are plotted. The elliptic flow rises with increasing transverse momentum. In Figure 4.15 and Figure 4.17, the results from the simulations compared to the experimental data for $\pi^{\pm}$ and $K^{\pm}$ at $\sqrt{s_{NN}} = 5.02$ TeV are depicted. For the case of kaons, the resuls agree with data up to 1.7 GeV in p_t. Nevertheless, some statistical irregularities in the figures can be seen. These irregularities are cause by the fact of small number of particles and problems with statistical fluctuations. Figures 4.29 and 4.30 show comparison between simulations with Trento2d and Trento3d.

The elliptic flow fluctuation are large at investigated energies. The fluctuation increase with increasing centrality and p_t. In summary, Figures 4.18 to 4.23 provides insight into the behaviour of the elliptic flow and its fluctuations as a function of p_t and centrality in heavy-ion collisions. It highlights the dominance of flow fluctuations at high p_t and the need for a comprehensive understanding of the underlying physics to accurately model the observed phenomena. The experimental physics group in the Niels Bohr Institute, Copenhagen, Denmmark, suggested new correlation function, which distinguish flow fluctuation in the angle and magnitude. These new correlation function are based on subevents method. From the published results by ALICE collaboration, it is clearly seen that fluctuation increase with p_t. Our result indicate qualitatively the same kind of behaviour. In the future, the current work will be extended by the study of flow fluctuation of angle and magnitude.

Bibliography

[1] G. Aad et al., *Phys. Lett. B* 710 (2012), pp. 363–382.

[2] K. Aamodt et al., *Phys. Rev. Lett.* 105 (2010), p. 252302.

[3] E. Abbas et al., *Phys. Lett. B* 726 (2013), pp. 610–622.

[4] B. Abelev et al., *Phys. Rev. C* 88.4 (2013), p. 044909.

[5] B. Abelev et al., *Phys. Rev. C* 88 (2013), p. 044910.

[6] B. Abelev et al., *JHEP* 06 (2015), p. 190.

[7] S. Acharya et al., *JHEP* 09 (2018), p. 006.

[8] S. Acharya et al., *Phys. Rev. C* 101.4 (2020), p. 044907.

[9] J. Adam et al., *Phys. Rev. Lett.* 116.13 (2016), p. 132302.

[10] J. Adam et al., *Phys. Lett. B* 772 (2017), pp. 567–577.

[11] L. Adamczyk et al., *Physical Review Letters* (Apr. 2014).

[12] G. Agakishiev et al., *Phys. Rev. C* 86 (2012), p. 014904.

[13] I. Bearden B. Tomášik F. Sannino and T. Dossing. "Hydrodynamic description of relativistic collisions", *Kobenhavns Universitet, Niels BohrInstitutet* (2004).

[14] I. Bearden B. Tomášikk F. Sannino and T. Dossing. "Topics in modern nuclear physics: Flow and Sizes", *Kobenhavns Universitet, Niels BohrInstitutet* (2004).

[15] R. S. Bhalerao. "Relativistic heavy-ion collisions", *1st Asia-Europe-Pacific School of High-Energy Physics*. 2014, pp. 219–239. DOI: 10.5170/CERN-2014-001.219. arXiv: 1404.3294 [nucl-th].

[16] A. Bilandzic, R. Snellings, and S. Voloshin, *Phys. Rev. C* 83 (2011), p. 044913.

[17] A. Bilandzic et al., *Phys. Rev. C* 89.6 (2014), p. 064904.

[18] J. D. Bjorken, *Phys. Rev. D* 27 (1983), pp. 140–151.

[19] M. Bleicher et al., *J. Phys. G* 25 (1999), pp. 1859–1896.

[20] N. Borghini, P. Mai Dinh, and J. Y. Ollitrault, *Phys. Rev. C* 64 (2001), p. 054901.

[21] P. Bozek and R. Samanta, *Phys. Rev. C* 105.3 (2022), p. 034904.

[22] W. Broniowski, M. Rybczynski, and P. Bozek, *Comput. Phys. Commun.* 180 (2009), pp. 69–83.

[23] J. Cimerman et al., *Phys. Rev. C* 103.3 (2021), p. 034902.

[24] F. Cooper and G. Frye, *Phys. Rev. D* 10 (1974), p. 186.

[25] L. P. Csernai. *Introduction to relativistic heavy ion collisions*. 1994.

[26] W. Florkowski. *Phenomenology of ultra-relativistic heavy-ion collisions*. London: World Scientific, 2010. ISBN: 98-142-8066-6.

[27] P. Huo et al., *Phys. Lett. B* 777 (2018), pp. 201–206.

[28] W. Israel and J. M. Stewart, *Annals Phys.* 118 (1979), pp. 341–372.

[29] Iu. Karpenko, P. Huovinen, and M. Bleicher, *Comput. Phys. Commun.* 185 (2014), pp. 3016–3027.

[30] Iu. A. Karpenko et al., *Phys. Rev. C* 91.6 (2015), p. 064901.

[31] W. Ke. "Partonic transport model application to heavy flavor". PhD thesis. Duke U., 2020. arXiv: 2001.02766 [nucl-th].

[32] W. Ke et al., *Phys. Rev. C* 96.4 (2017), p. 044912.

[33] Z. Lin et al., *Phys. Rev. C* 72 (2005), p. 064901.

[34] Z. Lin et al., *Phys. Rev. C* 72 (2005), p. 064901.

[35] C. Loizides, J. Kamin, and D. d'Enterria, *Phys. Rev. C* 97.5 (2018). [Erratum: Phys.Rev.C 99, 019901 (2019)], p. 054910.

[36] G. Ma and Z. Lin, *Phys. Rev. C* 93.5 (2016), p. 054911.

[37] J. S. Moreland, J. E. Bernhard, and S. A. Bass, *Phys. Rev. C* 92.1 (2015), p. 011901.

[38] J. Scott Moreland, Jonah E. Bernhard, and Steffen A. Bass, *Phys. Rev. C* 101.2 (2020), p. 024911.

[39] Stanislaw Mrowczynski and Edward V. Shuryak, *Acta Phys. Polon. B* 34 (2003), pp. 4241–4256.

[40] E. G. Nielsen and You Zhou. "Transverse momentum decorrelation of the flow vector in Pb-Pb collisions at $\sqrt{s_{NN}}$ = 5.02 TeV", (Nov. 2022). arXiv: 2211.13651.

[41] "Observation of flow angle and flow magnitude fluctuations in Pb-Pb collisions at $\sqrt{s_{\mathrm{NN}}}$ = 5.02 TeV at the LHC", (June 2022).

[42] T. Poledníček. *Application of relativistic fluid dynamics for the description of heavy ion collisions*. 2021.

[43] P. Romatschke and U. Romatschke. *Relativistic Fluid Dynamics In and Out of Equilibrium – Ten Years of Progress in Theory and Numerical Simulations of Nuclear Collisions*. 2019. arXiv: 1712.05815 [nucl-th].

[44] A. Schäfer et al., *Eur. Phys. J. A* 58.11 (2022), p. 230.

[45] B. Schenke, S. Jeon, and C. Gale, *Phys. Rev. Lett.* 106 (2011), p. 042301.

[46] Ch. Shen et al., *Comput. Phys. Commun.* 199 (2016), pp. 61–85.

[47] H. Song. "Causal Viscous Hydrodynamics for Relativistic Heavy Ion Collisions". Other thesis. Aug. 2009. arXiv: 0908.3656 [nucl-th].

[48] I. Štoll, J. Tolar, and I. Jex. *Klasická teoretická fyzika*. Praha: Univerzita Karlova, nakladatelství Karolinum, 2017. ISBN: 978-80-246-3545-3.

[49] I. Štoll, J. Tolar, and I. Jex. *Teoretická fyzika*. Praha: Česká technika - nakladatelství ČVUT, 2008. ISBN: 978-80-01-04005-8.

[50] M. Strickland. "Anisotropic Hydrodynamics: Three Lectures", *Acta Physica Polonica B* 45 (Oct. 2014). DOI: 10.5506/APhysPolB.45.2355.

[51] Schaefer T. *Quantum Chromodynamics: Computational Aspects*. 2016. arXiv: 1608.05459 [nucl-th].

[52] K. Tuchin. "Particle Production in Strong Electromagnetic Fields in Relativistic Heavy-Ion Collisions", *Advances in High Energy Physics* 2013 (June 2013). DOI: 10.1155/2013/490495.

[53] J. Weil et al., *Phys. Rev. C* 94.5 (2016), p. 054905.

[54] W. Zhao, H. Xu, and H. Song, *Eur. Phys. J. C* 77.9 (2017), p. 645.

[55] W. Zhao et al., *Phys. Rev. Lett.* 128.2 (2022), p. 022302.